Understanding the Caviahue-Copahue volcanic complex through kinematic solutions, paleotensors and analogue modelling

Nicolás Vigide [a,b,*], Daniel Yagupsky [c], Hernan Barcelona [c], Mariano Agusto [c], Alberto Caselli [b,d]

[a] *Observatorio Argentino de Vigilancia Volcánica (OAVV), Servicio Geológico Minero Argentino (SEGEMAR), Argentina*
[b] *Consejo Nacional de Investigaciones Científicas y Técnicas (CONICET), Argentina*
[c] *CONICET- IDEAN, Instituto de Estudios Andinos "Don Pablo Groeber", Universidad de Buenos Aires, Argentina*
[d] *Universidad Nacional de Río Negro. Instituto de Investigación en Paleobiología y Geología. Río Negro, Argentina*

ABSTRACT

This work aims to study the interaction between two of the most representative structural systems controlling the Caviahue-Copahue volcanic complex. To achieve this objective, a structural analysis based on outcrop-scale fault-slip data field surveys and analogue models were carried out. The deformation regime acting on the studied area was characterized, and the associated paleostresses were obtained from the kinematic data inversion.

The performed analysis in Caviahue-Copahue volcanic complex allowed to define two main sets of faults controlling the deformation of the area: NE-SW to ENE-WSW, and WNW-ESE to NW-SE, respectively. The first group comprises high-angle normal faults, resulting in a horst-and-graben setting with along-strike lengths up to 2 km. The second group shows strike-slip kinematics with a minor normal component. These NW-SE faults are related to the Miocene-Pliocene fissure-related volcanism and define the major caldera axis direction. In the geothermal area, the obtained paleostress orientation shows a consistent vertical σ1, denoting a local extensional regime. Regarding the geothermal field, the NE-SW extensional fault system is proposed as the main circulation pathways for hydrothermal fluids rising to the surface. The major NW-SE faults would act as barriers for this circulation.

The set of analogous experiments was used to contrast the obtained local structural kinematic results. Two non-coaxial extensional events were established to achieve a local scale approach to the structural configuration observed in the area. Simulations aimed to understand the structural behavior of the superposition of non-coaxial extensive events; they allowed us to assess the role of the different fault sets surveyed in the field within the system. Particularly, our findings support that the NW-SE-oriented structures compartmentalize the subsequent NE-SW-oriented faults, acting on occasions as transfer zones.

1. Introduction

The evolution of a volcanic system is usually complex and controlled by the interaction between regional and local factors such as the stress field, the governing structures, the dynamics of the magma chambers, the elasto- and visco-plastic state of the overlying rocks and the surficial characteristics of each eruptive center, among others. Shallow structures and stress fields exert a decisive control on magma and hydrothermal fluid circulation (e.g., Nakamura, 1977; Sibson, 1996; Tibaldi, 2005; Cembrano and Lara, 2009; Sánchez et al., 2013; Tardani et al., 2016; Sielfeld et al., 2017; Veloso et al., 2019; Pearce et al., 2020), as well as

deformation and destabilization of volcanic building flanks (e.g., Ventura et al., 1999; Siebert, 2002; Maccaferri et al., 2017).

The relationship between shallow crust structures and volcanism can be clearly observed throughout the entire Southern Volcanic Zone of the Andean Ridge (Cembrano and Lara, 2009). Convergence between Nazca and South American plates is slightly oblique and establishes a dextral regime, with a rate of 7–9 cm/year, which has prevailed for the past 20 Ma for the 33°–46° S (e.g., Pardo-Casas and Molnar, 1987; Somoza, 1998; Angermann et al., 1999). This regime facilitates the development of NNE-SSW and NE-SW structures and reactivation of NW-SE Andean transverse faults (Cembrano and Lara, 2009; Sánchez et al., 2013;

Pérez-Flores et al., 2016; Piquer et al., 2019).

Particularly, between 37° and 38° S, an accommodation zone is generated between two transpressive systems (Folguera et al., 2004; Melnick et al., 2006), and the Caviahue-Copahue volcanic complex is developed in this sector (37° 51′ S, 71° 02′ W). This volcanic complex is located 30 km east of the current volcanic arc front (Fig. 1). The most remarkable morphological feature inside the Caviahue-Copahue volcanic complex is the Agrio caldera, which constitutes a semi-rectangular depression of 300 km^2, with a N80°W major axis direction (Fig. 2). Another remarkable morphological feature is the current Copahue stratovolcano, located in the southwest extreme of the caldera, with activity during the last two decades (Fig. 2; Delpino and Bermúdez, 1993; Naranjo and Polanco, 2004; Petrinovic et al., 2014; Caselli et al., 2016; Tassi et al., 2017). It presents nine aligned craters in a NE-SW direction and hydrothermal manifestations of great interest, being one of the most studied geothermal resources in Argentina (e.g., Pesce, 1989; JICA-EPEN, 1992; Sierra et al., 1992; Mas et al., 1995, 1996; Varekamp et al., 2009; Mas, 2010; Tassi et al., 2017; Barcelona et al., 2019, 2020, 2021).

Considering that the detailed recognition of the structures associated with volcanic systems can reduce the possible scenarios of volcanotectonic hazards and contribute to the exploration of geothermal resources, this study explores the relationship between the local structures, the stress field, and the geothermal fluid circulation paths for the Caviahue-Copahue volcanic complex. First, inversion of kinematic indicators measured at outcrop scale faults was carried out. Second, the results were correlated with a series of analogous models, where overlapping

non-coaxial extensive events were established to achieve a local scale approach to the structural configuration observed in the area. These models allowed us to comprehend the role of the early-formed structures on the younger ones.

2. Caviahue-Copahue volcanic complex geological settings

2.1. Tectonic setting

2.1.1. Liquiñe-Ofqui fault zone

The Liquiñe-Ofqui fault zone is a 1200 km long intra-arc transient fault system (Fig. 1; Hervé, 1976, 1994; Cembrano and Hervé, 1993; Thomson, 2002). It is composed of NNE-SSW strike-slip faults with dextral kinematics, associated with NE-SW-trending faults with normal and dextral kinematics. This spatial arrangement forms duplex and horsetail geometries at the southern and northern extremes, respectively (Cembrano and Lara, 2009; Rosenau et al., 2006). Furthermore, the Liquiñe-Ofqui fault zone controls the occurrence, distribution and geometry of the major stratovolcanoes along its strike (Fig. 1; Lara et al., 2008; Cembrano and Lara, 2009; Sielfeld et al., 2017).

According to Cembrano et al. (2000), the Liquiñe-Ofqui fault zone registers ductile deformation with a dextral component between 6 and 3 Ma. From 1.6 Ma, a brittle deformation is recorded on the surface through dextral strike-slip structures (Lavenu and Cembrano, 1999). According to GPS data, the current activity of the fault system could absorb about 6.5 mm/year of the forearc northward displacement (Wang et al., 2007).
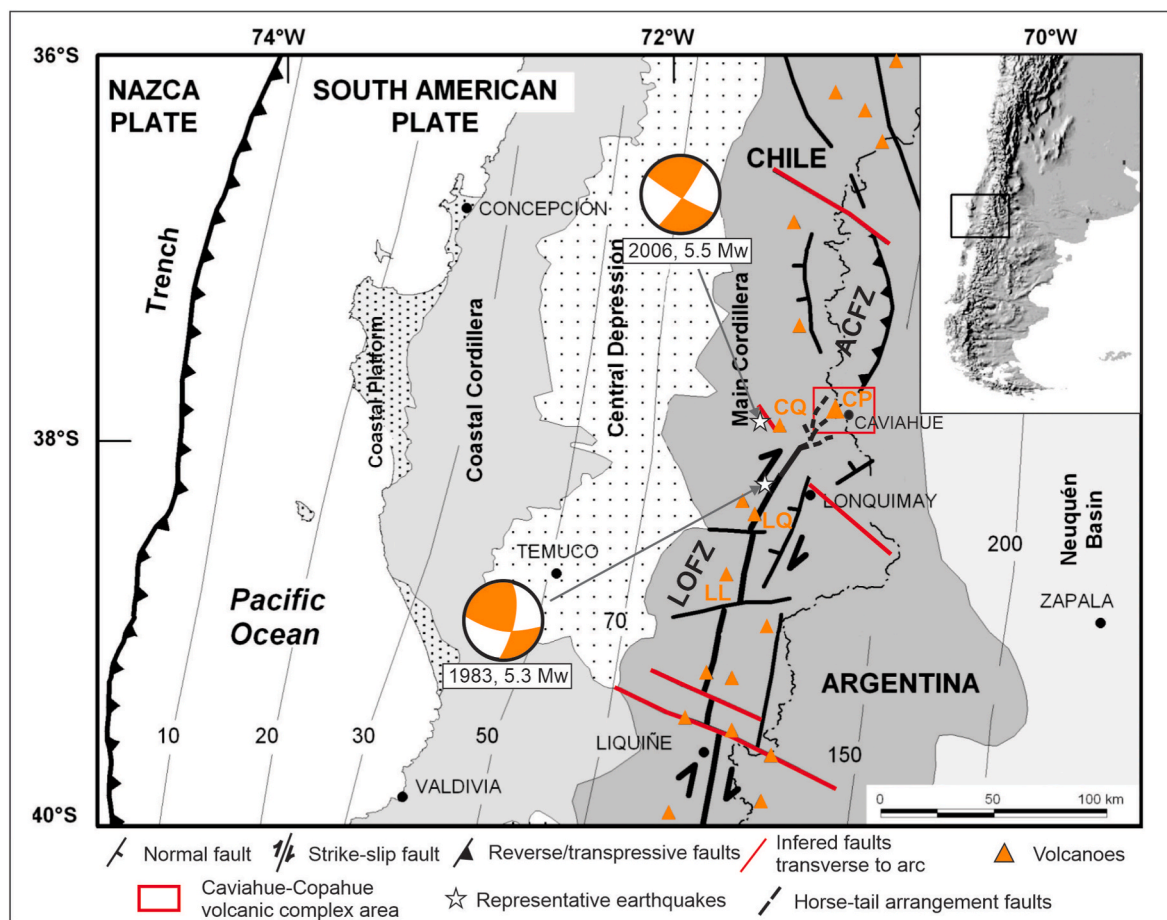

Fig. 1. Regional map where main morphotectonic units and fault systems are represented. (Melnick et al., 2006; Pérez-Flores et al., 2017). LOFZ: Liquiñe-Ofqui Fault Zone; ACFZ: Antiñir-Copahue Fault Zone. CP: Copahue volcano; CQ: Callaqui volcano; LQ: Lonquimay volcano; LL: Llaima volcano. Orange focal mechanisms (lower hemisphere, compressional quadrants) are taken from Barrientos and Acevedo (1992) and Global Centroid-Moment Tensor (GCMT), indicating year and magnitude. Modified from Melnick et al. (2002).
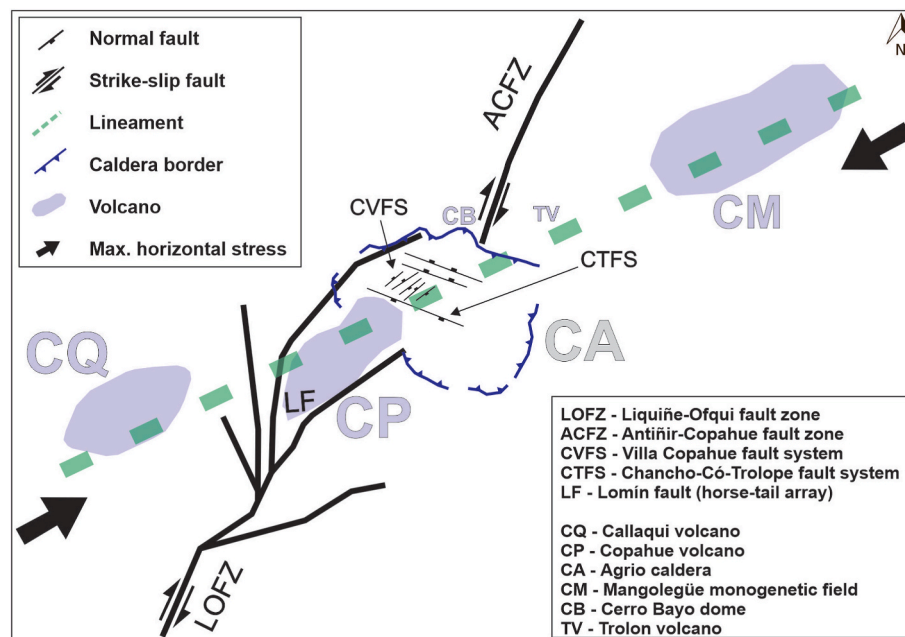
Fig. 2. Schematic structural setting of the Callaqui-Copahue-Mandolegüe lineament and the associated fault systems. Modified from Melnick et al. (2006).

The Liquiñe-Ofqui fault zone rotates clockwise in the northern extreme, distributing deformation in a "horsetail" faults spatial arrangement (the Lomín Fault; Figs. 2 and 3; Melnick et al., 2006). This arrangement is composed of NE-SW-trending faults parallel to the Lomín River, approximately 25 km long, which ends in the southwestern sector of the Agrio caldera (Figs. 1 and 2). According to Melnick et al. (2006), these horsetail faults present transtensive kinematics, originating the depression where El Barco lake is located (Fig. 3).

2.1.2. Andean transverse faults

The Andean transverse faults are a series of oblique-to-the-arc discrete faults that present a WNW-ESE to NW-SE-trends (Fig. 1; Sánchez et al., 2013). These series are inherited faults prior to the generation process of the Andean ridge (Radic, 2010), which may influence Quaternary volcanism in the Central and Southern Andes (Tibaldi, 2005; Acocella and Funiciello, 2006; Cembrano and Lara, 2009). Remote sensing, geophysical data and field evidence suggest that they play a significant role as lithospheric-scale structural elements in depth (Yáñez et al., 1998; Sánchez et al., 2013), with active sinistral kinematics confirmed by seismic data (Haberland et al., 2006; Aron et al., 2013). According to Pérez-Flores et al. (2016), these structures constitute large fault zones where big hydrothermal fluids reservoirs are hosted, developing fracture networks associated with mineral precipitation. Stanton-Yonge et al. (2016) indicate that NW-SE-oriented cortical faults have the potential to accommodate deformation resulting from oblique subduction, up to 0.9 mm/year and 1 mm/year of sinistral- and reverse displacement, respectively.

2.1.3. Antiñir-Copahue fault zone

Another fault system related to the caldera is the Antiñir-Copahue fault zone (Folguera et al., 2004). This system is located in the northern sector of the caldera (Figs. 1 and 2) and is defined as a dextral transpressive fault system. Folguera et al. (2004) determine three segments of approximately 30 km each long 90 km of its regional trace: a northern sector, composed of dextral transpressive faults; a central sector, characterized by dextral transtension, with subordinate transpressive faults; and a complex southern sector, where minor transpressive structures and major transtensive depocenters coexist.

2.1.4. Callaqui-Copahue-Mandolegüe lineament and local fault systems

The Callaqui-Copahue-Mandolegüe is a 60 km long NE-SW-trending transverse to the arc lineament, composed by the amalgamation of several volcanic centers (Fig. 2; Folguera et al., 2004, 2016; Melnick et al., 2006; Rojas-Vera et al., 2009; Radic, 2010): from west to east they are the Callaqui volcano, the Copahue volcano, the Trolón volcano, the Cerro Bayo dome, and the monogenetic fields of El Huecú and Mandolegüe. Two well-developed faults systems stand out within the Agrio caldera: the NE-SW-oriented Copahue village normal fault system (Bonali et al., 2016; Lundgren et al., 2017; Vigide et al., 2017; Barcelona et al., 2019, 2020; Lamberti et al., 2019) and a NW-SE-trending faults set, named Chancho-Có-Trolope fault system in this work (Fig. 2). Folguera et al. (2004) and Melnick et al. (2006) interpreted the Copahue village fault system as a transfer zone that would respond to the deformation between the dextral strike-slip of the Liquiñe-Ofqui fault zone, and the transpression produced by the Antiñir-Copahue fault zone (Fig. 1). On the other hand, Melnick et al. (2006) interpreted sinistral kinematics for the Chancho-Có-Trolope fault system, based on the parallelism with regional Andean transverse faults structures. Moreover, recent work on local seismicity suggests sinistral strike-slip displacement for the NW-SE structures (Montenegro et al., 2021). Both fault systems have a tectonic origin and were locally reactivated due to volcanotectonic movements (Mon, 1987). Their relative age was first established by Mon (1987), considering its relations to the geomorphological features produced by the pleistocene glaciation. This author concludes that an early structuration responsible for the Chancho-Có-Trolope fault system affected a first glacial abrasion surface, while younger movements produced very fresh scarps affecting a younger Pleistocene glacial pavement (NE-SW striking faults of the Copahue village fault system). Recently, Barcelona et al. (2020) confirmed this relative timing based on field observations, stating that the Chancho-Có-Trolope fault system formed before the extrusion of the Pleistocene ignimbrites, while the other set of NE-trending structures affect the ignimbrites of the Las Mellizas Formation (Mon, 1987; Pesce, 1989; JICA-EPEN, 1992). Furthermore, interferometric data indicate local movements associated with the NE-SW striking faults (Vélez et al. 2011; Lundgren et al., 2017).
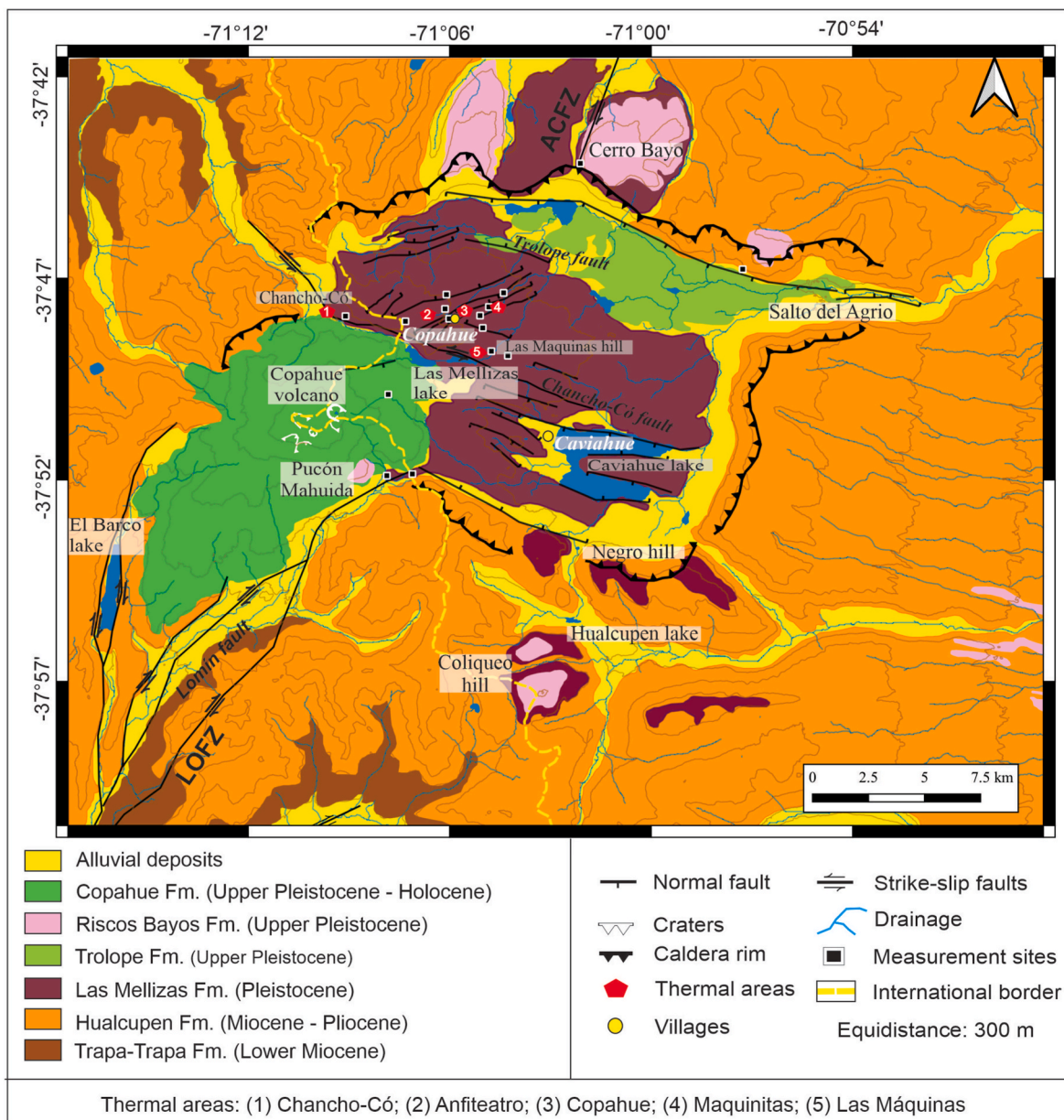
Fig. 3. Geologic map of the Caviahue-Copahue volcanic complex. Modified from Melnick et al. (2006) and Sruoga and Consoli (2011).

2.2. Stratigraphic framework

The structural basement in this area is composed of lower Tertiary sedimentary and volcanic rocks, known as the Andesitic Series (Groeber, 1956; Rapela and Llambías, 1985). For Oligocene to Miocene period, the area was controlled by extensional basins of continental rift origin, mainly infilled with pyroclastic rocks (Carpinelli, 2000; Jordan et al., 2001; Folguera et al., 2003; Burns et al., 2006; Radic, 2010). Sin-rift deposits are represented by sedimentary and volcaniclastic rocks from Cura-Mallín Formation (González and Vergara, 1962), followed by volcanic to volcaniclastic rocks of Trapa-Trapa Formation (Niemeyer and Muñoz, 1983; Suárez and Emparan, 1997).

The Trapa-Trapa Formation is unconformably overlayed by the pliocene volcanism of Cola de Zorro Formation in the Chilean sector (González and Vergara, 1962), known as Hualcupén Formation in Argentina (Pesce, 1989). It is locally interpreted as the result of fissure-related volcanism (Melnick et al., 2006; Sruoga and Consoli, 2011), without a defined central building. Linares et al. (1999) established K/Ar ages ranging between 5.6 and 4 Ma for these volcanic and volcaniclastic rocks. The Hualcupén Formation is associated with magnetic anomalies, which suggested NW-SE oriented feeder dikes (Rojas-Vera et al., 2008).

Middle-upper Pleistocene of the Agrio caldera is represented by the volcanic products of Las Mellizas Formation (Melnick et al., 2006). However, there are discrepancies between reported geochronologic ages from various authors. Linares et al. (1999) established K/Ar ages of 2.6 ± 1 Ma for the ignimbritic deposit of Las Mellizas Formation, while Sruoga and Consoli (2011) presented Ar/Ar ages of 125 ± 9 ka.

Following the K/Ar ages registered by Linares et al. (1999), the post-caldera volcanism is established after 1.2 Ma, conformed by fissure lavas of Trolope Formation (Pesce, 1989; Sruoga and Consoli, 2011), the associated acid domes of Riscos Bayos Formation (Melnick et al., 2006), and the development of the Copahue volcano (Delpino and Bermúdez, 1993; Melnick et al., 2006; Sruoga and Consoli, 2011).

2.3. Geothermal system

The geothermal field associated with the Copahue volcano comprises

five major manifestations: Copahue village, Anfiteatro, Las Maquinas and Maquinitas hot springs located NE of Copahue volcano. Chancho-Có thermal area is located 2.5 km north of the volcano, in Chilean territory. All hydrothermal zones are located over the topographic high delimited by the Trolope (to the north) and Chancho-Có faults (to the south; Fig. 3). In addition, these manifestations are located on Las Mellizas Formation and are characterized by intense acid-sulfated alteration and fumarolic activity (Groeber and Corti, 1920; Mon, 1987; JICA-EPEN, 1992; Sruoga and Consoli, 2011; Agusto et al., 2013; Barcelona et al., 2019).

This hydrothermal system is intrinsically associated with the high-angle normal faults of the Copahue village fault system (Mon, 1987; Bonali et al., 2016; Lundgren et al., 2017; Barcelona et al., 2019, 2020, 2021; Lamberti et al., 2019), which control the circulation of fluids. The Chancho-Có-Trolope fault system seems to compartmentalize the development of these normal faults (Barcelona et al., 2019, 2020).

3. Methodology

After a compilation of published structural maps (Melnick et al., 2006; Rojas-Vera et al., 2009; Bonali et al., 2016; Lamberti et al., 2019; Barcelona et al., 2020), a detailed structural field survey was performed. Both kinematic indicators at outcrop-scale faults and fractures were obtained at different sites inside the Agrio caldera. The reduced paleo-stress tensors for several sites were calculated by the inversion of the kinematic indicators. Finally, interpretations made on the structural evolution of the area were compared and validated by a series of analogue models addressing the overimposition of two non-coaxial extensional stages.

3.1. Fractures and faults sampling and kinematic analysis

A fractures-and-faults survey was carried out measuring fault planes at outcrop scale and, when possible, slip directions, following the recognition criteria introduced by several authors (Petit, 1987; Angelier, 1994; Doblas, 1998). These criteria are based on the determination of movement sense after recognizing kinematic indicators on a fault plane, such as slickensides, crystal fibers on slip planes, and associated Riedel fractures.

Principal strain axes were computed using the moment tensor summation method, using FaultKin software (Marrett and Allmendinger, 1990; Allmendinger et al., 2012). This software calculates each fault plane shortening and extension axes (P and T axes, respectively). The average kinematic solution for each fault population was also obtained using Linked Bingham Distribution statistical method (Marrett and Allmendinger, 1990), which allowed determining the directional maxima of the $\lambda 3$ and $\lambda 1$ strain axes. Unfolding correction was not applied because no evidence of significate blocks rotation was identified during fieldwork. Classification of the kinematic solutions and the automatic hierarchical clustering based on centroid and euclidean distances between the principal axes of the deformation tensors were performed using the FMC software (Álvarez-Gómez, 2019).

3.2. Stress inversion

The inversion method is based on the reconstruction of the stress field orientation, which generated the recognized faults system (Wallace, 1951; Bott, 1959; Angelier, 1984; Yin and Ranalli, 1993). From a kinematic compatible fault data set, four parameters of the reduced stress tensor are obtained, according to Angelier (1994): the principal stress axis σ1 (maximum compression), σ2 (intermediate compression) and σ3 (minimum compression), and the ratio of principal stress differences R = (σ2 - σ3)/(σ1 - σ3).

The Win-Tensor software (Delvaux, 1993) was employed to determine a reduced tensor by using an improved version of the Right Dihedral method of Angelier and Mechler (1977), and a

four-dimensional numeric rotational optimization (Delvaux, 1993). This last process involves the successive rotations of the tensor, testing equivalent configurations under the same R, until obtaining the minimum value of a misfit function (Miyouna et al., 2018). Once the relation R has been defined, the stress regime can be expressed numerically according to the definition of Delvaux et al. (1997), using an R' index which is convenient to compute the mean regional stress regime from a series of individual stress tensors in a given area.

This software determines the quality of the obtained tensor based on the amount and orientation of fault-plane dispersion in a data set. Four defined quality ranges can be determined, from A (good) to D (unreliable). In many cases, the software can indicate an E quality that does not imply that the results are not acceptable, but rather that the program considers that the requirements to validate the confidence are not given. In the case of the Caviahue-Copahue volcanic complex case, we use the inversion fault populations with at least 10 compatible faults, resulting in more reliable tensors.

3.3. Experimental methodology

3.3.1. Model setup

After recognizing variations in the kinematic solutions for the local structural domains, and analyzing their origin and their relationship with the main structures within the caldera, a series of analogous sand models were carried out. The particular objective of these experimental model series is to evaluate the structural control exerted by the faults array of an early extensional stage over subsequent structures, produced under an overimposed non-coaxial extensional stage. With these simulations, we intend to assess the structural role of the anisotropies imposed by the Chancho-Có-Trolope fault system over the most modern Copahue village fault system, and in particular, to unravel the genetic origin of both dextral and sinistral strike-slip fault plane solutions obtained associated with the Chancho-Có-Trolope fault system. At this point, it is important to note that the genesis of both fault systems was oversimplified by establishing pure extensional boundary conditions, which does not reflect the origin of these extensional arrangements. Most authors agree that transtension plays a key role in the described structural configuration. However, at the scale of interest, the simplification assumed is valid and allows us to analyze and evaluate possible structural evolutions, as will be discussed later.

The NW-SE normal faulting domain observed in the area corresponds to the Chancho-Có-Trolope fault system (Fig. 2), composed of faults with normal-oblique and normal kinematics related to fissure eruptive events that occurred during the Miocene-Pliocene (Melnick et al., 2006; Sruoga and Consoli, 2011). This structural setting was simulated in our models by the induction of an extensional event that gave rise to a set of well-developed sub-parallel normal faults, sub-perpendicular to the stretching direction imposed. Considering the normal kinematic solutions obtained for the younger NE-SW to ENE-WSW-oriented Copahue village fault system, a second stretching stage was overimposed on the previously developed normal-faults arrangement. The stretching direction applied formed an angle of 60° with the previous one, looking to reproduce the natural configuration of the study case.

A basal latex sheet was used to induce stretching to the overlying sand packet (Fig. 4a), reproducing the experimental approach taken in many previous kinds of research (Withjack and Jamison, 1986; Tron and Brun, 1991; McClay and White, 1995; Clifton et al., 2000; Clifton and Schlische, 2001; Bechis et al., 2014). A first layer of wet sand (5% H_2O by volume) was placed over the latex sheet to represent a stronger basement; this small amount of water allowed the sand to have greater cohesion than dry sand (Naylor et al., 1986; van Mechelen, 2004; Bechis et al., 2014). This sand package was covered by a less cohesive dry sand layer, simulating a sedimentary cover (Fig. 4b). The whole sand thicknesses established for the modelling came out from the idealized sequence in the area of the natural prototype. As mentioned before, the structural basement of the study area is composed of the Andesitic Series
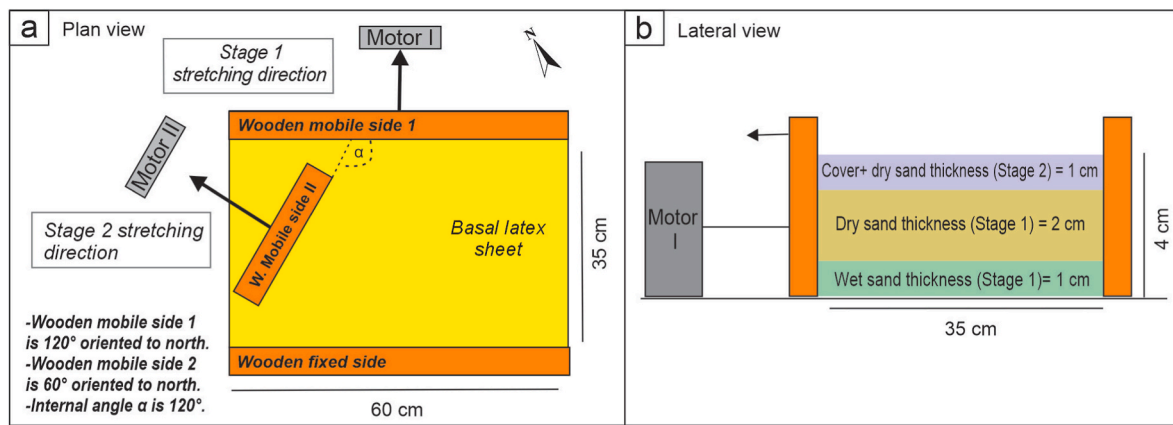
Fig. 4. Diagrams showing the configuration of the experimental apparatus and the used materials in (a) upper and (b) lateral views.

(Groeber, 1956; Radic, 2010), which is supposed to have a different mechanical behavior than the weaker cover rocks (Heap et al., 2016; Farquharson et al., 2017; Heap and Violay, 2021). This last mechanical section includes the sinrift sequence of Cura-Mallín and Trapa-Trapa Formations, represented by a 2 cm thick dry sand layer, and the volcanic and volcaniclastic deposits of the Hualcupén and Las Mellizas formations, simulated by the upper 1 cm thick layer of the model (Fig. 4).

A basal latex sheet of 35 cm wide by 60 cm long was used, with attached side walls (Fig. 4a). One of them was connected to a computer-controlled motor, allowing the latex to stretch, while the opposite wall was fixed to the modelling table. The basal latex sheet purpose is to uniformly transfer the deformation to the cover (Withjack and Jamison, 1986), simulating the upper section of a ductile lower crust (Withjack and Jamison, 1986; Bechis et al., 2014). The north direction in the experiments was chosen to get a reference frame where the stretching direction of stages I and II were N30° and N150°, respectively (Fig. 4a). This configuration eases the correlation of the resulting fault arrays with the main fault systems of the Agrio caldera: the Chancho-Có-Trolope fault system and the Copahue village fault system.

A 1 cm thick layer of wet sand was placed over the elastic latex sheet (Fig. 4b). Above, well sorted dry quartz sand with well-rounded grains, smaller than 300 μm and density (ρ) around 1400 kg/m^3, was mechanically sieved to get a 2 cm-thick package, reaching a total thickness of 3 cm (Fig. 4b). The first extensional pulse was then applied, pulling the moving side I at a constant rate of 0.05 mm s^{-1} until a final stretching of 5 cm (14%) was achieved (Fig. 4a). This extension was enough to generate observable fault scarps on the model surface. The resulting relief was covered with dry sand until a new horizontal surface was reached. Subsequently, sedimentation was completed until reaching 4 cm of the total thickness (Fig. 4b).

In order to prepare the model for the second extensional stage, two parallel lateral wooden sides were fixed to the latex sheet in tension, forming an angle of 60° concerning the other two wooden sides (Fig. 4a). The western side was displaced 3.8 cm (9.5% of extension) at a constant rate of 0.024 mm s^{-1}, while the other side remained fixed to the modelling table. In this way, the NW-SE applied stretching affected the oblique pre-existing normal faults network formed during stage 1; the relatively low amount of extension applied accounts for the incipient nature of the Copahue village fault system in the natural case (e.g., Bonali et al., 2016; Barcelona et al. al, 2019).

A fixed, high-resolution digital camera was used to photograph the top surface of the models at regular time intervals to study their map-view evolution. At the end of stage 1 of each experiment, their top surfaces were scanned with a high-resolution laser scanner, resulting in topographic maps with ~0.1 mm resolution. In addition, the digital photographs taken every 20 s were processed using optical image correlation techniques (PIV: particle imaging velocimetry). We used the

MatPIV v. 1.6.1 open-source software (Sveen, 2004) for MatLab ®, which allows quantifying the particle movements in materials subject to deformation based on image correlation techniques between two successive images (Adrian, 1991; White et al., 2001; Adam et al., 2005; Thielicke and Stamhuis, 2014). The correlation computes the most probable displacement for a group of particles within the established search windows between one image and another, in this case, 16 × 16 pixels (1 pixel = 0.4 mm of the model). The search areas were selected in 32 × 32 pixels and 16 × 16 pixels (1 pixel = 0.4 mm of the model). The PIV results were processed with the GEODEF 1.1 software (Yagupsky, 2010) to obtain incremental and cumulative deformation patterns. This analysis considers the directional derivatives for each incremental vector between two images and thus allows the calculation of an incremental deformation matrix for each point of the model surface. In this work, in order to best visualize the strain pattern evolution of the models surface, we used two strain parameters: the ellipticity (relationship between the major and minor axis of the deformation ellipse) for the incremental deformation, and the accumulated rotation (sum of the rotational component of each incremental deformation matrix) for the accumulated deformation.

3.3.2. Material properties and scaling

The selected dry sand presents density values between 1500 and 1730 kg/m^3, an angle of internal friction close to 33° and relatively low cohesion, C < 50 Pa (Yagupsky et al., 2008). van Mechelen (2004) showed that the dry sand cohesive strength could be increased by adding a small amount of liquid while other mechanical properties are preserved. The small amount of water incorporated into the sand volume was blended using a mixing machine for about 5 min. Slightly moistened sand (5% water by vol.) acquires a density of 1900 kg/m^3, an internal friction angle close to 40°, and a cohesion of 400 Pa (Bechis et al., 2014).

Models should satisfy the scaling equation proposed by Hubbert (1937), which relates the geometrical, kinematic and dynamic similarity between the model and nature. The models were scaled so that 1 cm of the experiment represents 1 km in the field, that is, L* = 1 × 10^{-5}. The density relationship between the granular materials (1200–1900 kg m^{-3}) and natural rocks (2600–3300 kg m^{-3}) is ρ* ~0.5. Also, both the model and the natural prototype are subjected to the same value of the gravity acceleration (g* = 1). Considering that the natural rocks cohesion values range from 15 to 110 MPa (Schellart, 2000), granular materials with cohesion between 50 and 400 Pa are appropriate for the simulations. This responds to the stress relationship obtained, σ* = ρ* x g* x L* = 6 × 10^{-6}. Therefore, the materials used are appropriate as they satisfy the scaling criteria.

4. Results

4.1. Structural domains into the Agrio caldera

Based on the main structures recognized in the Agrio caldera (Mon, 1987; JICA-EPEN, 1992; Melnick et al., 2006; Barcelona et al., 2019, 2020), it is possible to define two major structural domains. The most relevant structural domain (named the Chancho-Có-Trolope fault system; Fig. 2) is composed of ~WNW-ESE oriented faults, with traces of several kilometers in length. These structures may occasionally display ~ NW-SE inflections, as in the case of the Chancho-Có fault (Fig. 5). This domain has a regional development, crossing the caldera from east to west with occurrences to north and south. The most essential morphostructural lineaments belonging to this domain are found in the western and southern sectors of the caldera, where they define the Caviahue lake horseshoe shape and the southern caldera rim (Fig. 5). According to the bibliography, these structures recorded oblique or normal kinematics related to fissure eruptive style events that occurred during Miocene-Pliocene (Melnick et al., 2006; Sruoga and Consoli, 2011).

The second important domain is the Copahue village fault system, composed by NE-SW to ENE-WSW-oriented structures (Fig. 5). They seem to have a restricted development within the caldera area (Fig. 2), between the Chancho-Có and Trolope faults to north and south respectively (Fig. 5). Outside the caldera, in the southwestern sector, this orientation is represented by segments of Lomín fault (Fig. 5), while no structures with these strikes are identified to the east of the caldera.

It is important to note that the hydrothermal manifestations of the Caviahue-Copahue volcanic complex are found in the Copahue village fault system domain, delimited both to the north and south by ~ NW-SE lineaments (Fig. 5). It was also observed that a NNW-SSE-oriented lineament crosses the north flank of the Copahue volcano, connecting the Chancho-Có thermal zone, the Copahue volcano active crater and the Pucón Mahuida dome (Fig. 5). This trace restricts the development of the ~WNW-ESE structures towards the western sector of the study area.

4.2. Fractures direction and kinematic analysis

From the survey of kinematic fault data, a total of 180 fault planes and 111 fractures were measured in 15 sites (Figs. 5 and 6; Appendix 1). First, the outcrop-scale fault populations yielded three dominant direction trends (Fig. 6d): NE-SW to ENE-WSW, NNE-SSW, and NW-SE. In addition, fractures show three main trends: NE-SW, ENE-WSE and NNW-SSE (Fig. 6d). Over 75% of these structures have dips greater than 70° (Fig. 6e), in good agreement with measurements made by Barcelona et al. (2019) and field observations performed by other authors (Mon, 1987; Lundgren et al., 2017; Roulleau et al., 2017).

The existence of fault sets that yield more than one solution could indicate the presence of heterogeneities (Marrett and Allmendinger, 1990). Several solutions can be obtained with homogeneous subpopulations that meet the requirement of kinematic compatibility. In particular, two solutions (a and b) were obtained on sites 8, 10, 12, 14 and 15. Of the total kinematic indicator data for the Caviahue-Copahue volcanic complex, a minority of them were eventually discarded due to their poor quality or the dispersion of the fault data at each station. Kinematic analysis is summarized in Table 1.

Twenty solutions with the corresponding principal strain axes have been computed for the 15 sites, widely distributed in different sectors of the caldera. The Karevina diagram (Kaverina et al., 1996; Kagan, 2005) was used to rank the kinematics of each solution (Fig. 7). A total of eight solutions were classified as normal, three as normal-strike-slip, two as strike-slip normal, two as strike-slip, four as strike-slip reverse and one as reverse strike-slip. These solutions were subjected to automatic
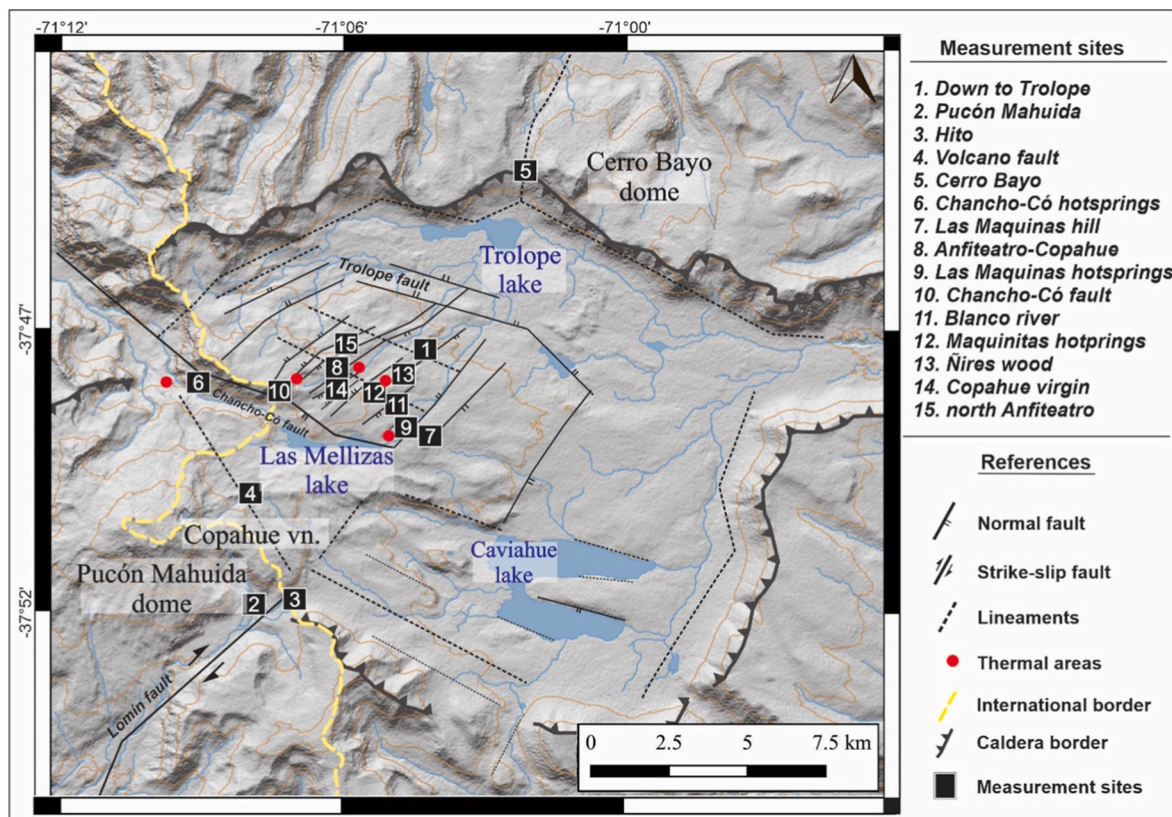

Fig. 5. Structural settings of Caviahue-Copahue volcanic complex, taken from Barcelona et al. (2019). Measure sites are indicated with black boxed numbers. Location of thermal areas taken from JICA-EPEN (1992).
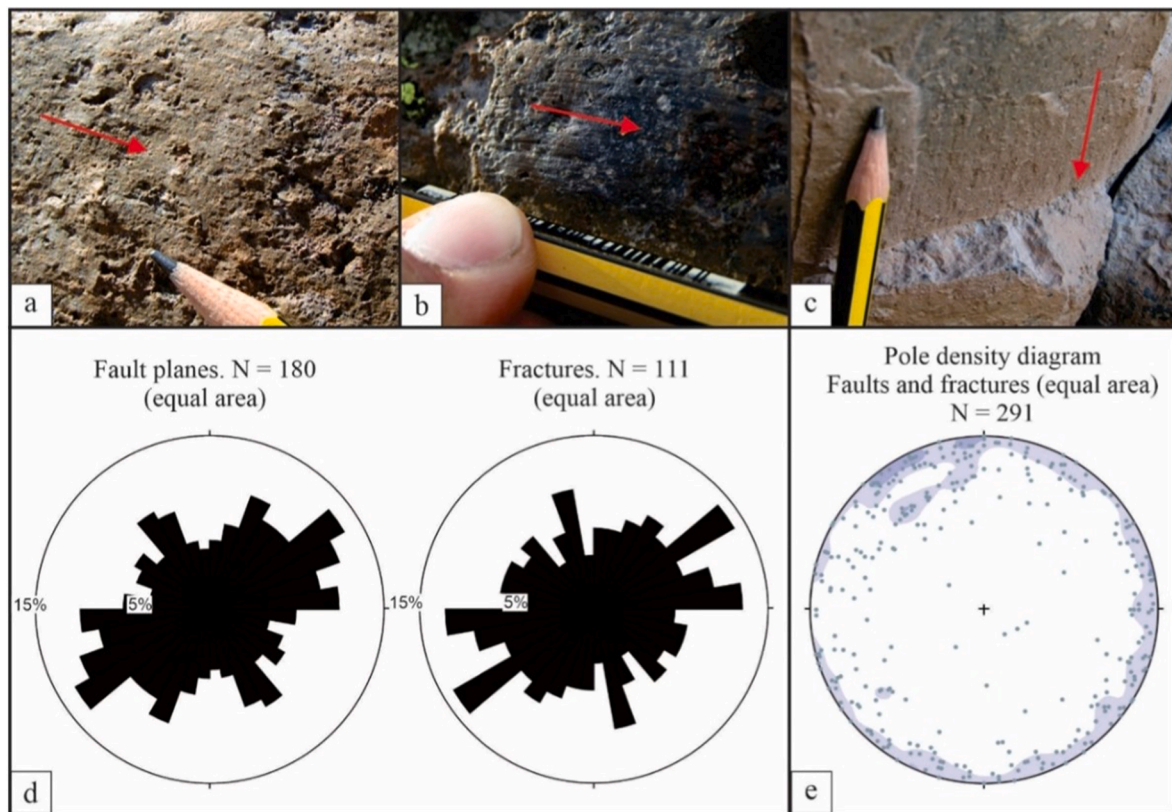
Fig. 6. (a, b, c) Steps and striation in Las Mellizas Formation. Red arrows indicate the kinematic sense. (d) Rose diagrams of fault planes and fractures population measured at 15 sites. (e) Pole density diagram of fractures and faults population.

hierarchical classification (Álvarez-Gómez, 2019), and five groups were obtained, which are described below.

Fig. 8 shows the spatial distribution of the kinematic solutions over a shaded DEM with the main structures. The most representative group is composed of eight normal kinematic solutions (sites 1, 2, 4, 7, 9, 10a, 12a and 14a) that spread through the NNE flank of the Copahue volcano and in the geothermal field within the caldera (Fig. 8). Solutions from sites 7, 10a, 12a and 14a, and sites 1 and 9 have a null B-axis that correlates with NE and NNE trending faults, respectively; both are part of the Copahue village fault system. On the other hand, sites 2 and 4 have a null B-axis that correlates with an NNW-trending lineament towards the southwest of the caldera.

Site 3, placed at the international passage of Pucón Mahuida, shows a reverse solution with a minor right-lateral strike-slip component. This solution corresponds with a transpressive local regime, where the shortening axis is sub-horizontal and oriented in the NE direction. The extensional axis, also sub-horizontal, is oriented in the NW direction.

Normal solutions with minor strike-slip components are mostly placed at the Chancho-có, Anfiteatro-Copahue and Las Maquinitas geothermal zones (sites 6, 8a and 13, respectively). Sites 8a, between Anfiteatro and Copahue, and 13, immediately north of Las Maquinitas, are associated with a NW-trending fault with a minor left-lateral strike-slip component. Chancho-có (site 6) and northern Copahue (site 15a) geothermal zones are associated with a NE-trending fault system. However, while in the former the strike-slip component is minor, in the latter it is dominant.

In the north of the caldera, site 5 shows a right-lateral strike-slip solution, with an N–S-oriented extension axis and an E-W-oriented shortening axis, both sub-horizontal. Although it is formed by few data, this NE-trending faults array is associated with a regional structure near the Cerro Bayo dome (Fig. 5), constituting the southern end of the dextral strike-slip Antiñir-Copahue fault zone. Two other strike-slip

solutions were defined immediately north (site 15 b) and south (14 b) of the village of Copahue. The former has an NNW-SSE-oriented shortening axis consistent with a left-lateral displacement, and the latter has a WNW-ESE-oriented shortening axis with a right-lateral displacement. These solutions are structurally associated with the NE- ENE-trending faults of the Copahue village fault system, as will be discussed later.

Four strike-slip – reverse solutions were obtained; interestingly, they are distributed along WNW-ESE structural trends inside the geothermal field. The solutions from sites 11 and 8 b, located between Las Maquinitas and Las Maquinas and between Anfiteatro and Copahue hydro-thermal zones, respectively, are pretty similar, with NW-SE-oriented shortening axis and NE-SW-oriented extension axis. Also, the kinematic solution at the Chancho-có fault (site 10 b) is characterized by an NW-SE-oriented shortening axis. Finally, site 12 b presents a strike-slip – reverse solution with NE-SW-oriented shortening and NW-SE-oriented extension axis at the Las Maquinitas hydrothermal zone. Despite the dispersion of the shortening-extension axis orientations between solutions, all these low representative statistical solutions (sites 8 b, 10 b and 12 b) define similar kinematics, suggesting that they may be representing a reactivation of pre-existing anisotropies not ideally oriented for accommodating the overall deformation.

We interpret that most of the solutions with dominant strike-slip kinematics obtained inside the caldera (e.g., 8 b, 10 b, 11, 12 b, 14 b and 15 b) reflect the lateral movement of transfer zones of the Copahue village fault system, probably reactivating pre-existing WNW-ESE underlying faults of the Chancho-Có-Trolope fault system; this will be further analyzed with analogous models (Section 5.3) and discussed (Section 6).

4.3. Stress inversion results

Stress inversion was carried out in those populations with more than

Table 1

Fault plane solution data for the 15 measurement sites in the Caviahue-Copahue volcanic complex area (see map on Fig. 5 for sites location). n/nt is the selected fault number concerning the total data for each station. λ3: shortening axis, λ2: null axis; λ1: extension axis.

| Site	Name (rock Formation)	Solution	n/nt	λ3	λ2	λ1
1.	Down to Trolope (Las Mellizas Fm.)	**a**	**5/6**	55/ 094	13/ 203	32/ 301
2.	Pucón Mahuida (Copahue Fm.)	**a**	**10/ 11**	78/ 271	09/ 134	08/ 043
3.	Hito (Las Mellizas Fm.)	**a**	**6/8**	24/ 213	32/ 319	47/ 093
4.	Volcano fault (Copahue Fm.)	**a**	**14/ 18**	52/ 228	24/ 353	27/ 096
5.	Cerro Bayo (Las Mellizas Fm.)	**a**	**3/4**	14/ 097	67/ 226	17/ 002
6.	Chancho-Có hotsprings (Las Mellizas Fm.)	**a**	**4/5**	45/ 023	42/ 230	14/ 128
7.	Las Maquinas hill (Las Mellizas Fm.)	**a**	**6/7**	54/ 307	01/ 039	36/ 130
8.	Anfiteatro-Copahue (Las Mellizas Fm.)	**a**	**11/ 18**	49/ 075	39/ 271	08/ 174
		b	**5/ 18**	06/ 341	53/ 244	37/ 076
9.	Las Maquinas hotsprings (Las Mellizas Fm.)	**a**	**9/ 11**	74/ 074	07/ 191	14/ 283
10.	Chancho-Có fault (Las Mellizas Fm.)	**a**	**9/ 16**	60/ 123	16/ 243	25/ 340
		b	**5/ 16**	01/ 357	52/ 088	37/ 266
11.	Blanco river (Las Mellizas Fm.)	**a**	**7/9**	07/ 150	54/ 250	35/ 055
12.	Las Maquinitas hotsprings (Las Mellizas Fm.)	**a**	**19/ 31**	59/ 315	05/ 054	31/ 147
		b	**6/ 31**	14/ 217	44/ 113	43/ 320
13.	Ñires wood (Las Mellizas Fm.)	**a**	**4/6**	45/ 099	42/ 303	12/ 202
14.	Copahue virgin (Las Mellizas Fm.)	**a**	**10/ 17**	56/ 292	15/ 046	29/ 145
		b	**7/ 17**	22/ 107	66/ 314	10/ 201
15.	North Anfiteatro (Las Mellizas Fm.)	**a**	**9/ 15**	32/ 284	52/ 066	19/ 182
		b	**6/ 15**	12/ 353	78/ 171	01/ 262
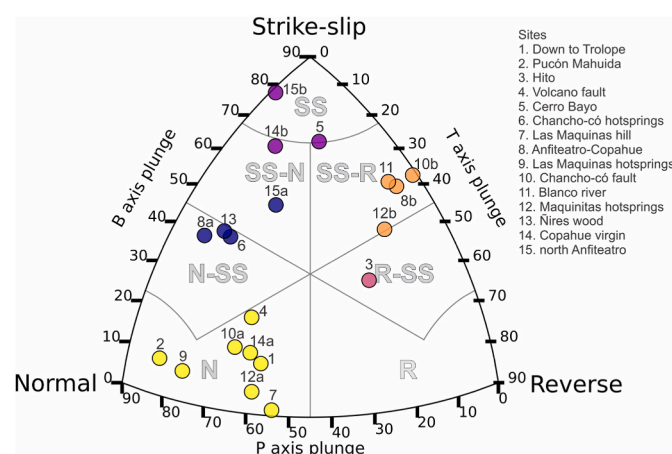
Fig. 7. Kaverina classification based on the principal axes of shortening (λ3), null (λ2) and extension (λ1) of the strain tensor solutions on Table 1 (Kaverina et al., 1996; Kagan, 2005). The shading of the symbols represents the groups of focal mechanisms resulting from the hierarchical clustering analysis. N: Normal; N-SS: Normal – Strike-slip; SS-N: Strike-slip – Normal; SS: Strike-slip; SS-R: Strike-slip – Reverse; R–SS: Reverse – Strike-slip; R: Reverse. Plot and clustering performed with FMC software (Álvarez-Gómez, 2019).

10 fault data, which fulfilled the kinematic compatibility necessary to consider homogeneous faulting (Wallace, 1951; Bott, 1959). An initial dataset, equal to or greater than 10 compatible faults, assures a more reliable result (e.g., Delvaux, 2003). The stress inversion results are reported in Table 2 and Fig. 9. Data were excluded during processing to obtain a better fit with the largest possible data set. When more than four faults are excluded, they are not discarded; instead, they are arranged in a subset for a new calculation of another stress tensor. Five consistent paleostress tensors were obtained, all of them extensional.

Site 2 is located in the southeastern part of the Copahue volcano. A paleotensor compatible with a sub-vertical σ1, a N–S sub-horizontal σ2, and an E-W-oriented sub-horizontal σ3 was obtained (Fig. 9). This configuration describes a radial extensional regime, with an R' = 0.14 and a "D" quality. The maximum principal stress orientation coincides with the obtained P-axis position in the kinematic solution (Fig. 8).

On the northeastern flank of the volcano, site 4 also indicates a radial extensional regime, with a sub-vertical σ1, a NNE-SSW-oriented sub-horizontal σ2, and a NW-SE-oriented horizontal σ3 (Table 2 and Fig. 9). Compared with the kinematic solution obtained for this site, the maximum and minimum stresses orientations roughly coincide with the respective deformation axes (P and T).

A pure extensional stress regime is recorded for site 8, located between the Copahue village and Anfiteatro thermal manifestation; the σ1 direction is sub-vertical, σ2 is sub-horizontal, trending ENE-WSW, and the σ3 is horizontal and NNW-SSE-oriented (Table 2 and Fig. 9). Concerning the main kinematic solution obtained for this site (8a in Fig. 8), σ3 direction is parallel to the T-axis. In addition, the maximum horizontal stress (SHmax) direction is in good agreement with the regional SHmax (azimuth 060°) obtained by Lavenu and Cembrano (1999) towards the south of the Caviahue-Copahue volcanic complex, using an inverse microfault analysis. Rosenau et al. (2006) estimated the same azimuth by analyzing volcanic centers elongation and dikes directions at the northern end of the Liquiñe-Ofqui fault zone.

In Maquinitas hotsprings, east of the Copahue village (site 12), the slip inversion gives rise to a sub-vertical σ1, a NNE-SSW-oriented σ2, and a NW-SE-oriented, gently dipping σ3 (Table 2 and Fig. 9). This configuration indicates a radial extensional regime, with R' = 0.19, suggesting a relatively low magnitude of σ2. The maximum (σ1) and minimum (σ3) principal stress directions coincide with the P and T-axis ones of the main kinematic solution obtained for this site (12a in Fig. 8), respectively.

Finally, site 14 reveals a radial extensional regime for the Copahue village area. The σ1 is sub-vertical; σ2 is sub-horizontal and oriented NNE-SSW, while σ3 is sub-horizontal and oriented NW-SE. The maximum and minimum stress orientations coincide with those obtained for P and T axes of the main faults set of this site, respectively (14a in Fig. 8).

The obtained paleostress configurations are consistent as a whole with a pure to radial extensional regime, with a NE-SW to ENE-WSW-oriented SHmax. Sites 8, 12 and 14 are associated with the Maquinitas, Villa Copahue and Anfiteatro thermal areas (Fig. 9). Lamberti et al. (2019) and Barcelona et al. (2019) established that the rise of fluids in these thermal zones are directly linked to the normal faults of the Copahue village fault system. The slight differences found between the local SHmax obtained and the regional SHmax reported in the literature may be a consequence of the overpressure of geothermal fluids that slightly deviate the direction of the stress field (e.g., Magee and Zoback, 1993; Sibson, 1996; Sibson and Rowland, 2003).

4.4. Analogue models results and discussion

The first fault scarps developed after 1-cm stretching have NW-SE direction, normal to the applied extension. They were located near the mobile edge, probably due to a higher initial stretching of the latex sheet. The formation of these faults gave rise to an incipient horsts-and-grabens array (Fig. 10). After 5 cm of mobile wall displacement, the
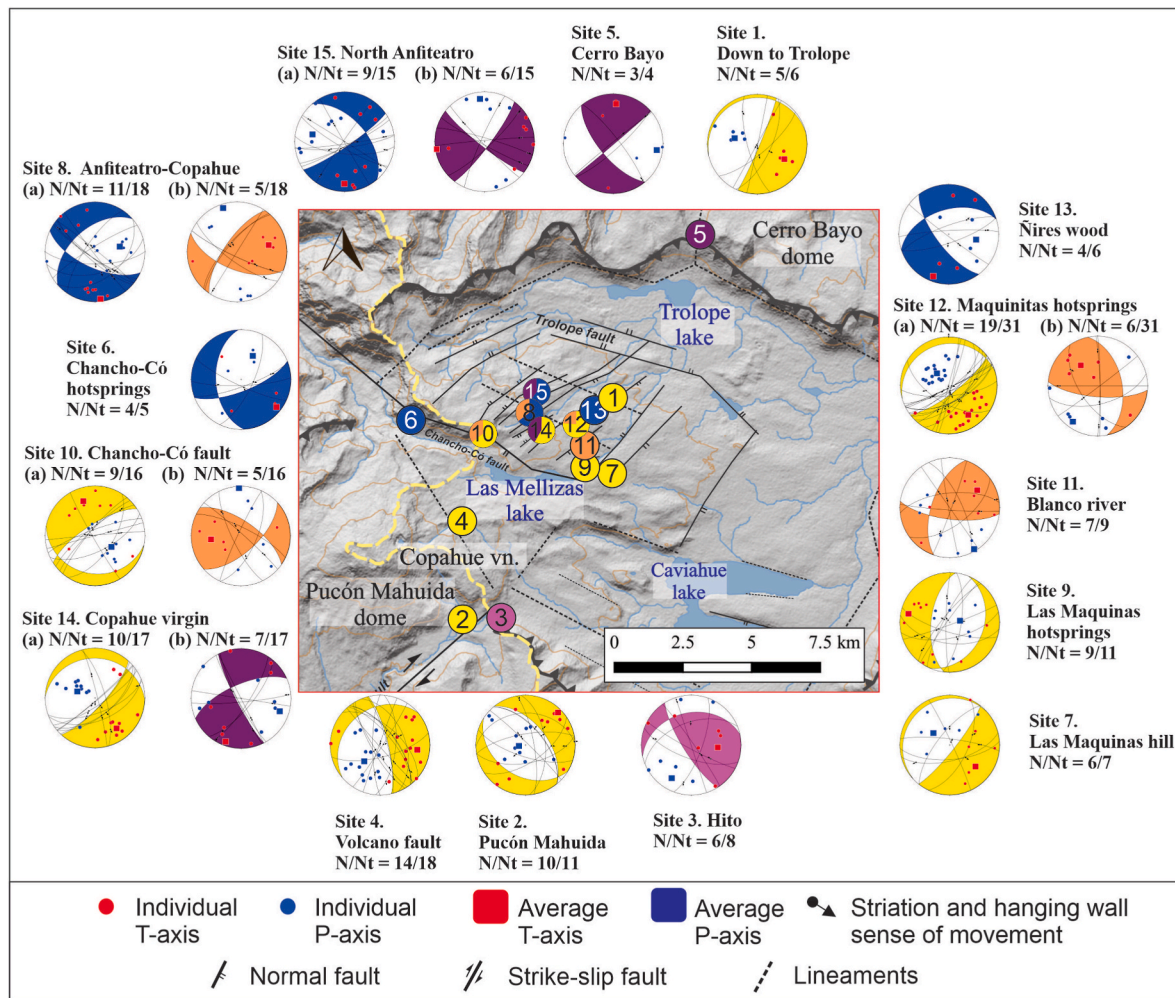
Fig. 8. Kinematic results of the Caviahue-Copahue volcanic complex (equal area and lower hemisphere projection, compressional quadrants shown in white). Color of each solution represents the obtained groups after the automatic clustering analysis performed (see Fig. 7).

Table 2
Paleostress tensors from fault-slip data for the Caviahue-Copahue volcanic complex. n = number of measurements used for the inversion; nt = total number of processed measurements; σ1, σ2, σ3 = plunge and azimuth of principal stress axes; R = (σ2 - σ3)/(σ1 - σ3); R' = stress regime index; α = average misfit angle.

Site	Name	Location	n/nt	σ 1	σ 2	σ 3	R	R'	α	Regime	Quality
2.	Pucón Mahuida	37°52′51″S 71°08′48″W	**6/10**	72/010	17/172	05/264	0.14	0.14	13.9	Radial extension	D
4.	Volcano fault	37°51′17″S 71°07′56″W	**10/14**	53/212	37/035	01/304	0.11	0.11	38.3	Radial extension	E
8.	Anfiteatro-Copahue	37°48′51″S 71°06′13″W	**11/11**	81/095	08/247	04/337	0.38	0.38	54	Pure extension	C
12.	Las Maquinitas hotsprings	37°49′10″S 71°05′26″W	**17/19**	69/287	02/022	21/112	0.19	0.19	47.2	Radial extension	C
14.	Copahue virgin	37°49′14″S 71°06′08″W	**9/10**	65/243	19/023	15/118	0.15	0.15	51.4	Radial extension	D

extensional faults system and associated relief were fully defined (Fig. 10a). The early-formed fault segments connected with each other, giving rise to greater length traces. Relay zones were also generated, due to the overlap of normal fault segments with either the same or opposite vergence.

At the end of stage 1, the model was covered with horizontal dry sand layers until reaching 4 cm of the total thickness. In stage 2, a new stretching direction was imposed at 60° from the initial one (Fig. 10b). After reaching 1.2 cm of displacement, the first normal faults with short length (between 2 and 5 cm) became visible, close to the moving wall (Fig. 10b).

After 2.4 cm of displacement, the NE-SW to ENE-WSW faults propagated laterally, covering the southern part of the interest area (Fig. 10c). The length of these structures was close to 5 cm; some showed slight curvatures at their ends, probably responding to border effects. In

the western sector of the area, a minor WNW-ESE-striking fault was generated, with visible sinistral strike-slip displacement.

After 3.6 cm of stretch, a NE-SW-oriented, unevenly distributed horsts-and-grabens system developed (Fig. 10d). The longest faults reached about 12 cm in length. Some of them developed curved traces. Also, short WNW-ESE- and NNE-SSW-oriented strike-slip faults were recognized. The former group had sinistral movement, while the latter showed dextral movement. Besides, relay ramps between opposite vergence normal faults were registered.

By overlapping the structural maps of the first and second stages, it is observed that some first-stage structures limit the propagation of second-stage ones, giving rise to a compartmentalized normal faults array (Fig. 11a). By visual inspection, no reactivation of pre-existing oblique faults was registered during the latter extensional process.

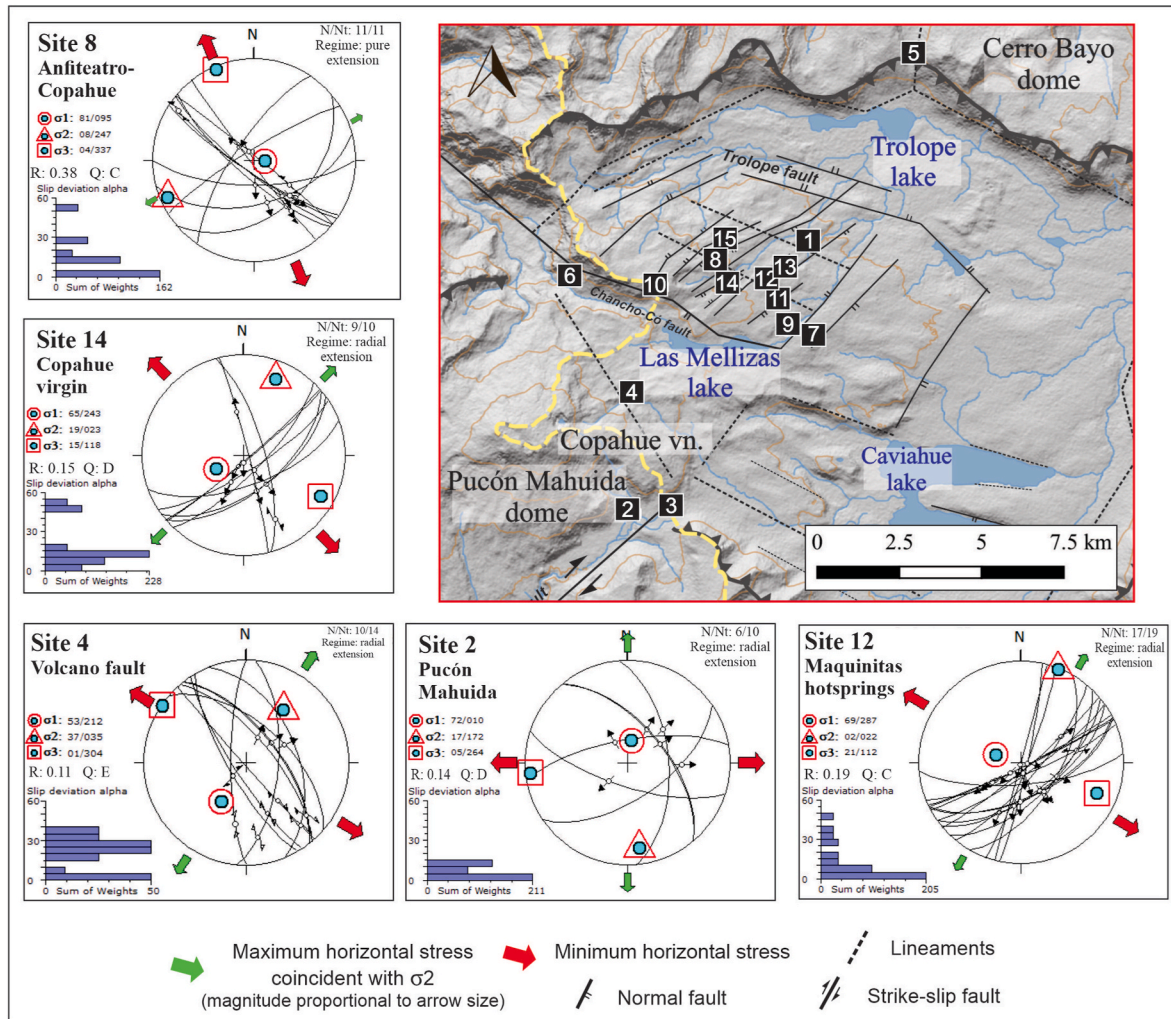However, the incremental ellipticity maps of Fig. 11b reveal that

Fig. 9. Stress inversion results for the Caviahue-Copahue volcanic complex, and its location. Lower-hemisphere Schmidt stereoplot of the fault-slip data subsets and corresponding stress tensor. Histogram of weighted misfit function. Major structures are shown in grey lines.

some NW-SE linear zones absorb incremental deformation, conforming relay zones between the second-stage normal faults. These zones coincide with the location of the main pre-existing structures, showing that discrete segments accommodate some deformation during stage 2. Also, ENE-WSW directions absorbing incremental strain are seen (see sector B in Fig. 11b), reflecting the active normal faults mapped on stage 2. Finally, NNE to N–S deformation zones are detected and interpreted as new transfer zones between the second-stage structures, since their direction is sub-perpendicular to them (i.e., parallel to the stretching direction).

Fig. 11c shows that the shear is accumulated in two particular zones. In sector A, NW-SE-oriented deformation zones predominate, associated with minor reactivations of previous extensional structures. However, in sector B, where there is a more significant development of normal faults generated during the second stage, NE-SW-trending structures absorb shear, displaying short NW-SE inflections. From this analysis, it is recognized that the initial structures of the model, which at first glance did not seem to reactivate, do so with strike-slip components linked to the transfer between active second-stage normal faults. These transfer zones express the structural heritage of the first structural stage of stretching. Therefore, these controls incorporate a strong imprint on the distribution and compartmentalization of the most recent structures, and their strike-slip kinematics is associated with the degree of obliquity between the applied stretch directions.

As is highlighted by similar experiments in previous works (Henza

et al., 2010, 2011; Ghosh et al., 2019), when there is an overlap of non-coaxial extensive events, with angles greater than 45° between both directions of stretching, the generation of the second-stage faults is compartmentalized by major first-stage faults. The same is observed during the initial to intermediate evolution of the second stage of our experiments (Fig. 11). Deformation concentrates over normal fault scarps and fault segments of the previous extensional stage that act as transfer zones for the active fault system. In advanced stages, deformation trends orthogonal to the direction of active stretching overimpose the previous structures, overcoming its structural control.

5. Discussion and local structural characterization

Kinematic structural analysis of fault-slip data was based on 15 measurement sites in the Caviahue-Copahue volcanic complex. Fault plane solutions have roughly NNE-SSW to ENE-WSW, WNW-ESE to NW-SE, and NNW-SSE trends. The solutions are rather consistent, with a predominance of normal strike-slip kinematics. They define an extensional deformation regime likely leading to the NE-SW to ENE-WSW Copahue village fault system development (Fig. 12). This extensional system is morphologically well developed within the Agrio caldera. It correlates with extrusions of volcanic products (Melnick et al., 2006; Sruoga and Consoli, 2011) and the main surficial expressions of the hydrothermal system (JICA-EPEN, 1992; Lamberti et al., 2019).

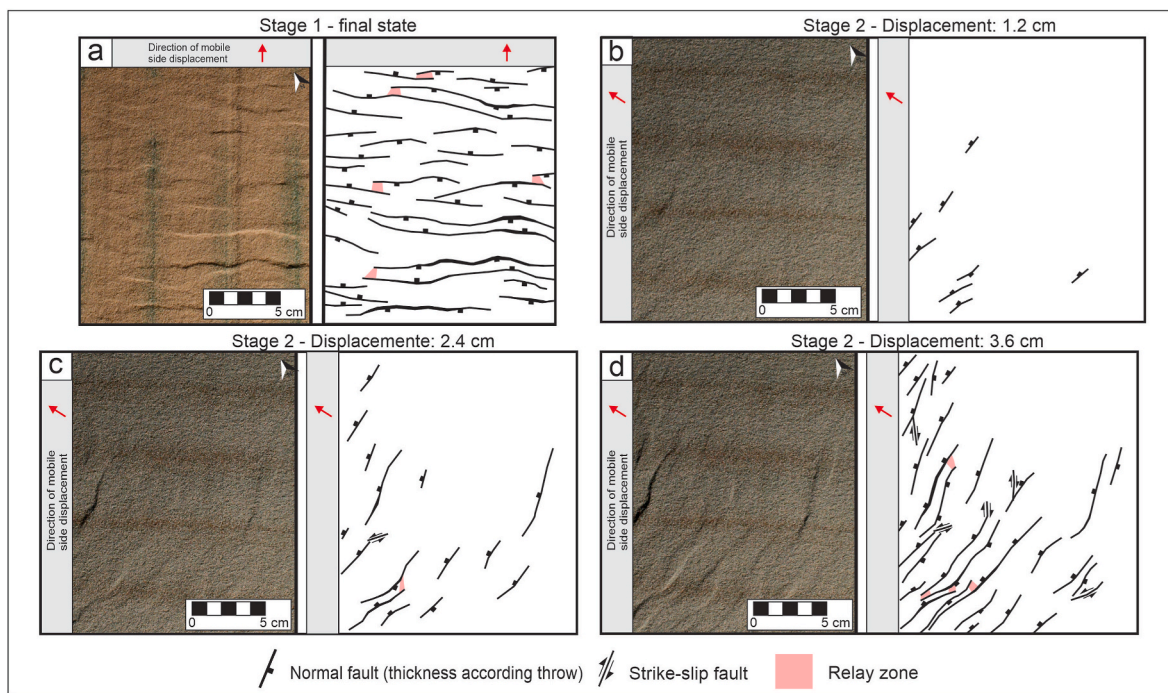Paleotensors computed near Copahue village and along the

Fig. 10. Stage 1: first extensional event; stage 2: second non-coaxial extensional event. (a) left: plan-view of the final state after the first extensional event; right: structural interpretation. (b, c, and d) left: plan-view photographs, taken in different moments of the second extensional stage; right: corresponding structural interpretation.
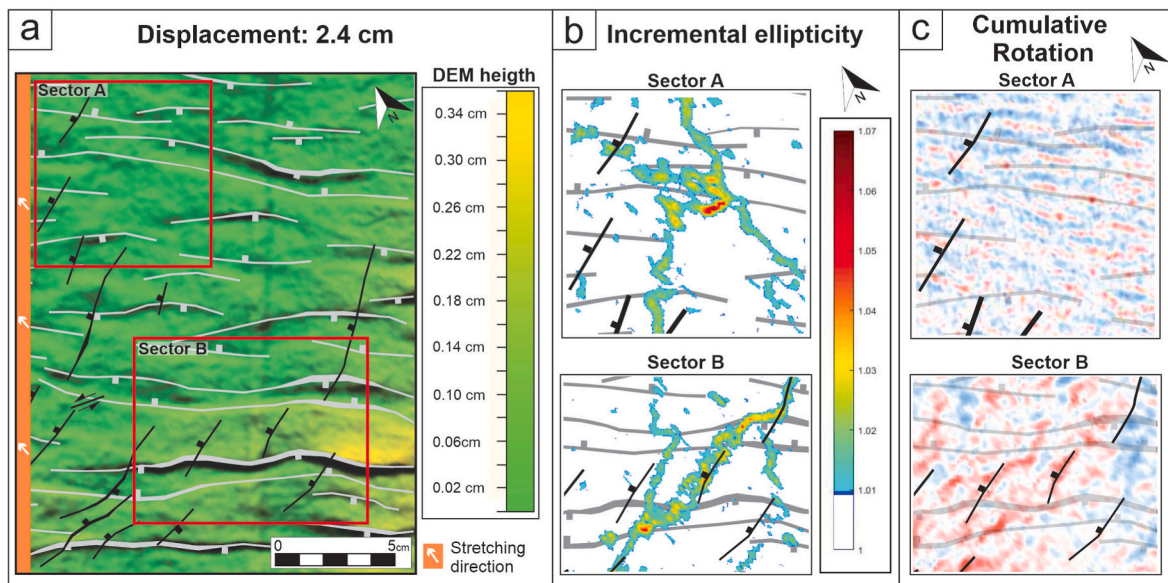

Fig. 11. (a) Structural map of stage 2 (in black), over the topography of the final state of stage 1; whose structures are mapped in grey. (b) Incremental ellipticity between successive pictures, calculated for 6% of extension, and (c) cumulative shear rotation in two sectors of the model (boxes in "a") after 2.4 cm extension during the second stage (blue = dextral shear rotation, red = sinistral shear rotation).

northeastern slope of the Copahue volcano define a local NE-SW to ENE-WSW-oriented SHmax, in good agreement with previous regional estimations (azimuth 060°; Lavenu and Cembrano, 1999). This direction agrees with the main trend of the Copahue village fault system; it is also consistent with the alignment of craters of Copahue volcano (Nakamura, 1977), with the Callaqui and Lonquimay volcanoes elongation axes, and with the alignment of other minor emission centers (Rosenau et al., 2006; Cembrano and Lara, 2009; Bertín, 2010; Sielfeld et al., 2017). Within the Caviahue-Copahue volcanic complex, this direction coincides with the lineaments which contain the Pucón Mahuida acid dome over

the southeastern sector of Copahue volcano, and the fissure vents of the Trolope Formation (Sruoga and Consoli, 2011).

A strike-slip kinematic solution is obtained in the Cerro Bayo dome, northeast of the caldera (Fig. 8). Although based on a poor fault-slip population, the E-W-oriented sub-horizontal P-axis express consistency with the southern end of the regional dextral strike-slip Antiñir-Copahue fault zone. On the other hand, the kinematic solution and paleostress results in volcanic areas (sites 2 and 4 placed on Pucón Mahuida dome and Copahue volcano, respectively; Fig. 9) could respond to volcanic building lithostatic load stress (Watanabe et al., 2002; Roman and
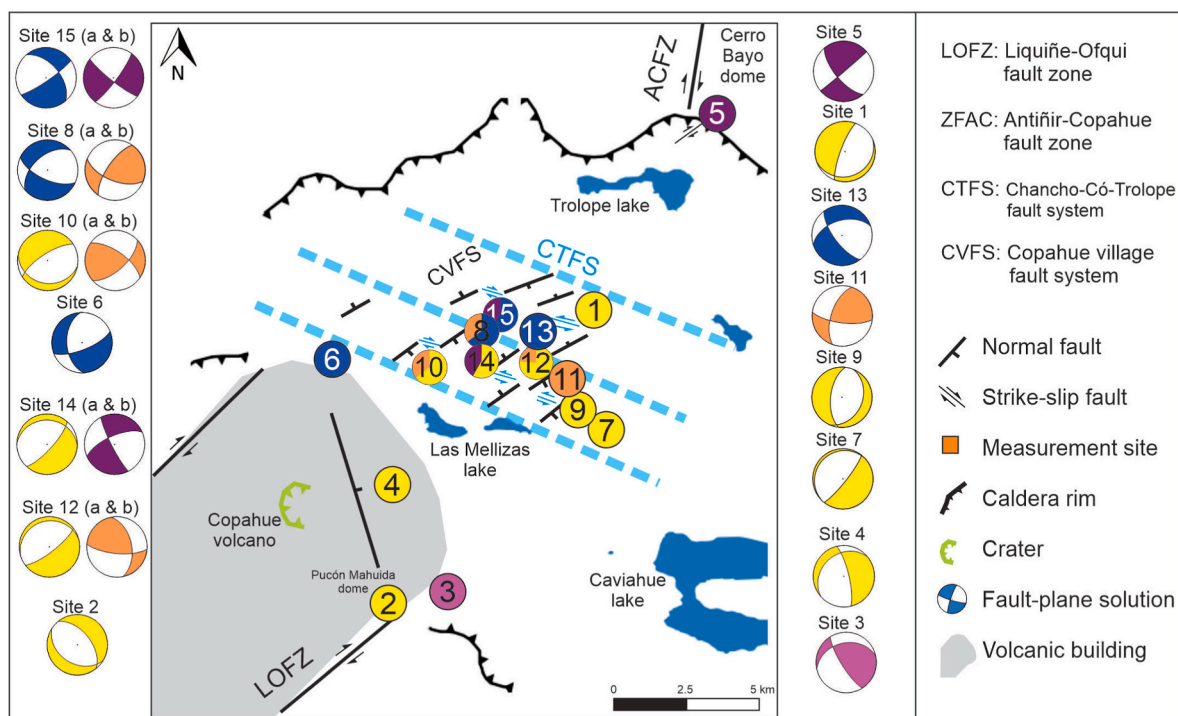
Fig. 12. Simplified diagram of the main fault systems in the thermal area of the Caviahue-Copahue volcanic complex, showing the kinematic solutions obtained for each site. Color of each solution represents the obtained groups after the automatic clustering analysis performed (see Fig. 7).

Jaupart, 2014; Maccaferri et al., 2014), where vertical shortening axis is expected to predominate. The influence of the inflation and deflation processes of the volcanic building (e.g., Vélez et al., 2011, 2016; Lundgren et al., 2017) over the local stress could not be ruled out.

It is interesting to note that the strike-slip - reverse kinematic solutions (8 b, 10 b, 11, 12 b; three of them right-lateral) and the pure strike-slip kinematic solutions (14 b and 15 b left- and right-lateral, respectively) coexist with the normal faulting regime and associated paleostress configuration obtained from the Copahue village fault system. Moreover, this fault system overimpose the previous WNW-ESE to NW-SE-oriented Chancho-Có-Trolope extensional fault system. Physical models where different extensional phases overlap, commonly non-coaxial (e.g., Badley et al., 1988; Sinclair, 1995; Boccaletti et al., 1998; Lepvrier et al., 2002; Huchon and Khanbari, 2003; Morley et al., 2004; Bellahsen et al., 2006), usually show that the pre-existing normal faults orientation significantly influences the development of subsequent normal faults setting (Henza et al., 2010, 2011; Ghosh et al., 2019). This influence impacts on (i) the faults linkage during reactivation, (ii) the displacement magnitude and direction of reactivated faults, and (iii) the attitude, length, and amount of newly-formed normal faults (Henza et al., 2010, 2011; Ghosh et al., 2019). The designed series of analogous models aim to achieve a local scale understanding of the observed structural configuration, analyzing, in particular, the role of structural heritage (the Chancho-Có-Trolope fault system) on the younger normal faults array of the Copahue village fault system.

The influence of the Chancho-Có-Trolope fault system as anisotropies on the subsequent development of the Copahue village fault system was simulated by two non-coaxial extensional events imposed on the analogue experiments. It is essential to clarify that the genesis of each fault system was oversimplified through the establishment of pure extensional boundary conditions. This does not imply that the studied prototype has suffered extensional tectonic configurations such as rift systems, but rather that it is intended to achieve a local response linked to larger-scale processes. Therefore, the first simulated stage corresponds with the extensional deformation episode registered by the Chancho-Có-Trolope fault system, probably caused by reactivations of

the Agrio caldera during the early Pleistocene (Melnick et al., 2006; Sruoga and Consoli, 2011). The synthetic normal faults system was subjected to a new extensional stage, simulating the local response to a major transtensive tectonic regime, associated with the inflection point of the Liquiñe-Ofqui fault zone at this latitude, under a NE-SW-trending SHmax since 1.6 Ma (Lavenu and Cembrano, 1999; Rosenau et al., 2006; Somoza and Ghidella, 2012).

Incremental ellipticity and cumulative rotation analyses for an intermediate displacement step of the second stretching stage revealed the activation of transfer zones between active normal faults, taking advantage of pre-existing normal faults (Fig. 11). Besides, these early structures restrict the lateral propagation of the second-stage fault traces, giving rise to a compartmentalized fault array. NW-SE and N–S to NNE-SSW transfer zones were also identified through the incremental strain mapping, in addition to the WNW-ESE ones (Fig. 11). They are sub-perpendicular to the main strike of the normal faults of the second stage, as expected for transfer faults without a pre-existing structural fabric. For relatively low angles (less than 45°) between both stretching directions, early-formed faults reactivate with strike-slip kinematics; this is consistent with similar studies that investigate the effect of a pre-existing oblique normal fault network on the geometry of the younger normal faults (Henza et al., 2010, 2011; Ghosh et al., 2019).

It should be noted that some uncertainty remains on the relative chronology between both structural systems, given the absence of reliable radiometric dating of key volcanic units of this area. The observation of cross-cutting relations between faults is not either possible, because of the different levels of exposures of the units affected. However, as mentioned in section 2, other sources of geological evidence can be invoked to sustain the proposed timing, in agreement with similar interpretations proposed by those authors (Mon, 1987; Pesce, 1989; JICA-EPEN, 1992; Melnick et al., 2006; Bonali et al., 2016; Barcelona et al., 2020). We therefore consider that the established order of deformation events applied in our experiments is so far the one with best constraints to establish a relevant analogy with the natural prototype.

These experimental results help to unravel the origin of the obtained kinematic solutions for the WNW-ESE to NW-SE structural domain

(Fig. 12), where the existence of fault segments with both sinistral and dextral kinematics would respond to the accommodation of fault-delimitated blocks under a local NW-SE extensional pulse, associated with the most recent transtensional regime that affect the study area.

6. Conclusions

An interpretation of the interaction between two of the most representative structural systems within the Agrio caldera was carried out with an exhaustive survey of kinematic fault data at outcrop-scale in 15 measurement sites, most of them at the Copahue geothermal field. Several kinematic solutions and paleostress tensors were obtained and analyzed, and the interpretations were performed using analogue models to unravel the genetic origin of the results and field observations.

The surveyed kinematic data yielded 20 fault-plane solutions. Two trends were mainly observed: an extensional deformation regime is revealed by NE-SW to ENE-WSW-oriented faults, together with strike-slip deformation along WNW-ESE to NW-SE-oriented faults. The solutions for the first faults group allowed us to validate the normal kinematics of the Copahue village fault system. During the most recent local extensional event, the second faults group (Chancho-Có-Trolope fault system) reactivated as transfer zones.

The stress inversion allowed us to obtain five paleostress tensors. They define a pure to a radial extensional regime with a subvertical $\sigma1$, favouring volcanic products extrusion and thermal areas occurrence. Four of the obtained paleostress configurations have NE-SW to ENE-WSW oriented maximum horizontal stress, subparallel to the regional one. The Copahue village fault system orientation is parallel to this maximum horizontal stress direction. It is regionally associated with the NE-SW regional transfer zone between the Liquiñe-Ofqui fault zone to the south of the caldera and the Antiñir-Copahue fault system to the north.

Results of the experimental models presented herein provide essential tools to understand the genesis of the recognized outcrop-scale structures and their kinematic solutions. They suggest that the obliquity between the two extensional episodes registered in the caldera (expressed by the Chancho-Có-Trolope fault system and Copahue village fault system) would have promoted the partial reactivation of the first NW-SE to WNW-ESE trending normal faults population as transfer and relay zones for the second-stage, NE-SW to ENE-WSW trending normal faults. Furthermore, models showed that the compartmentalization of the NE-SW to ENE-WSW faults responds to the heritage of the pre-existing normal faults array. The insights gained from this study may assist to future volcano-tectonic-related seismic events interpretation and improve our knowledge about the Copahue geothermal system.

CRediT authors statement

Nicolás Vigide: Writing – review & editing, Writing – original draft, Visualization, Validation, Investigation, Formal analysis, Data curation, Conceptualization. **Daniel Yagupsky:** Writing – review & editing, Supervision, Project administration, Methodology, Funding acquisition, Conceptualization. **Hernan Barcelona:** Writing – review & editing, Visualization, Funding acquisition, Conceptualization. **Mariano Agusto:** Writing – review & editing, Funding acquisition. **Alberto Caselli:** Writing – review & editing.

Declaration of competing interest

The authors declare that they have no known competing financial interests or personal relationships that could have appeared to influence the work reported in this paper.

Data availability

Data will be made available on request.

Appendix A. Supplementary data

Supplementary data related to this article can be found at https://doi.org/10.1016/j.jsames.2022.104136.

References

Acocella, V., Funiciello, R., 2006. Transverse systems along the extensional Tyrrhenian margin of central Italy and their influence on volcanism. Tectonics 25. https://doi.org/10.1029/2005TC001845.

Adam, J., Urai, J.L., Wieneke, B., Oncken, O., Pfeiffer, K., Kukowski, N., Lohrmann, J., Hoth, S., van der Zee, W., Schmatz, J., 2005. Shear localisation and strain distribution during tectonic faulting - new insights from granular-flow experiments and high-resolution optical image correlation techniques. J. Struct. Geol. 27, 283–301.

Adrian, R.J., 1991. Particle imaging techniques for experimental fluid mechanics. Annu. Rev. Fluid Mech. 23, 261–304.

Agusto, M., Tassi, F., Caselli, A.T., Vaselli, O., Rouwet, D., Capaccioni, B., Darrah, T., 2013. Gas geochemistry of the magmatic-hydrothermal fluid reservoir in the Copahue–Caviahue Volcanic complex (Argentina). J. Volcanol. Geoth. Res. 257, 44–56.

Allmendinger, R.W., Cardozo, N.C., Fisher, D., 2012. Structural Geology Algorithms: Vectors and Tensors. Cambridge University Press, Cambridge, England, p. 289.

Álvarez-Gómez, J.A., 2019. FMC—earthquake focal mechanisms data management, cluster and classification. Software 9, 299–307.

Angelier, J., 1984. Tectonic analysis of fault slip data sets. J. Geophys. Res. 89, 5835–5848.

Angelier, J., 1994. Fault slip analysis and palaeostress reconstruction. In: Hancock, P.L. (Ed.), Continental Deformation. Pergamon, Oxford, pp. 101–120.

Angelier, J., Mechler, P., 1977. Sur une méthode graphique de recherche des contraintes principales également utilisable en tectonique et en séismologie: 1a méthode des dièdres droits. Bull. Soc. Géol. France 7 (19), 1309–1318.

Angermann, D., Klotz, J., Reigber, C., 1999. Space-geodetic estimation of the nazca-south America euler vector. Earth Planet Sci. Lett. 171, 329–334.

Aron, F., Allmendinger, R.W., Cembrano, J., González, G., Yáñez, G., 2013. Permanent fore-arc extension and seismic segmentation: insights from the 2010 Maule earthquake, Chile. J. Geophys. Res. Solid Earth 118, 724–739. https://doi.org/10.1029/2012JB009339.

Badley, M.E., Price, J.D., Dahl, C.R., Agdestein, T., 1988. The structural evolution of the northern Viking Graben and its bearing upon extensional models of basin formation. J. Geol. Soc. 145, 455–472. London.

Barcelona, H., Yagupsky, D., Vigide, N., Senger, M., 2019. Structural model and slip-dilation tendency analysis at the Copahue Geothermal System: inferences on the reservoir geometry. J. Volcanol. Geoth. Res. 18–31. https://doi.org/10.1016/j.jvolgeores.2019.03.007.

Barcelona, H., Maffucci, R., Yagupsky, D., Senger, M., Bigi, S., 2020. Discrete fracture network model of the vapor zone leakages at the Copahue geothermal field. J. Struct. Geol. 140, 104155.

Barcelona, H., Senger, M., Yagupsky, D., 2021. Resource assessment of the Copahue geothermal field. Geothermics 90, 101987.

Barrientos, S., Acevedo, P., 1992. Seismological aspects of the 1988–1989 Lonquimay (Chile) volcanic eruption. J. Volcanol. Geoth. Res. 53, 73–87.

Bechis, F., Cristallini, E., Giambiagi, L., Yagupsky, D., Guzmán, C., García, V., 2014. Transtensional tectonics induced by oblique reactivation of previous lithospheric anisotropies during the Late Triassic to Early Jurassic rifting in the Neuquén basin: insights from analog models. J. Geodyn. 79, 1–17. https://doi.org/10.1016/j.jog.2014.04.010.

Bellahsen, N., Fournier, M., d'Acremont, E., Leroy, S., Daniel, J.M., 2006. Fault reactivation and rift localization: northeastern Gulf of Aden margin. Tectonics 25. https://doi.org/10.1029/2004TC001626.

Bertín, D., 2010. El complejo volcanico lonquimay y la zona de falla liquiñe-ofqui: estudio estructural, morfometrico y gravimetrico. Universidad de Chile.

Boccaletti, M., Bonini, M., Mazzuoli, R., Abebe, B., Piccardi, L., Tortrici, L., 1998. Quaternary oblique extensional tectonics in the Ethiopian rift (Horn of Africa). Tectonophysics 287, 97e116.

Bonali, F., Corazzato, C., Belloti, F., Groppelli, G., 2016. Active tectonics and its interactions with Copahue volcano. In: Tassi, F., Vaselli, O., Caselli, A. (Eds.), Copahue Volcano, pp. 23–45.

Bott, M.H.P., 1959. The mechanics of oblique slip faulting. Geol. Mag. 96, 109–117.

Burns, W.M., Jordan, T.E., Copeland, P., Kelley, S.A., 2006. The case for extensional tectonics in the Oligocene-Miocene Southern Andes as recorded in the Cura-Mallín basin (36°-38°S). In: Kay, S., Ramos, V. (Eds.), Evolution of an Andean Margin: A

Tectonic and Magmatic View from the Andes to the Neuquén Basin (35°-39°S lat.), vol. 407. Geological Society of America, Special Paper, pp. 163–184. https://doi.org/10.1130/206.2407(08.

Carpinelli, A., 2000. Análisis estratigráfico, paleoambiental, estructural y modelo tectono-estratigráfico de la Cuenca Cura-Mallín VIII y IX Región, Chile. Memoria de Título Inédito), Universidad de Concepción, Departamento de Ciencias de la Tierra, p. 158.

Caselli, A.T., Velez, M.L., Agusto, M., Liccioli, C., Vaselli, O., 2016. Prehistoric to Historic Volcanic Activity at Copahue Volcano. Copahue Volcano. Springer, pp. 175–198.

Cembrano, J., Hervé, F., 1993. The Liquiñe-Ofqui Fault Zone: a Major Cenozoic Strike Slip Duplex in the Southern Andes. Second ISAG, Oxford, UK, pp. 175–178.

Cembrano, J., Lara, L., 2009. The link between volcanism and tectonics in the southern volcanic zone of the Chilean Andes: a review. Tectonophysics 471 (1–2), 96–113.

Cembrano, J., Schermer, E., Lavenu, A., Sanhueza, A., 2000. Contrasting nature of deformation along an intra-arc shear zone, the Liquiñe–Ofqui fault zone, southern Chilean Andes. Tectonophysics 319, 129–149.

Clifton, A.E., Schlische, R.W., 2001. Nucleation, growth, and linkage of faults in oblique rift zones: results from experimental clay models and implications for maximum fault size. Geology 29, 455–458.

Clifton, A.E., Schlische, R.W., Withjack, M.O., Ackermann, R.V., 2000. Influence of rift obliquity on fault-population systematics: results of clay modeling experiments. J. Struct. Geol. 22, 1491–1509.

Delpino, D., Bermúdez, A., 1993. La actividad volcánica del volcán Copahue durante 1992. Erupción con emisión de azufre piroclástica. Provincia de Neuquén. XII Congreso Geológico Argentino (Mendoza), Abstracts 4, 292–301.

Delvaux, D., 1993. The TENSOR Program for Palaeostress Reconstruction: Examples from the East African and the Baikal Rift Zones. Terra Abstract, Abstract (Supplement No.1, to Terra Nova). 5 pp. 216.

Delvaux, D., Moeys, R., Stapel, G., Petite, C., Levi, K., Miroshnichenko, A., Ruzhich, V., San'kov, V., 1997. Paleostress reconstructions and geodynamics of the Baikal region, Central Asia. Part II: cenozoic tectonic stress and fault kinematics. Tectonophysics 282 (1–4), 1–38.

Doblas, M., 1998. Slickenside kinematic indicators. Tectonophysics 295 (1), 187–197. https://doi.org/10.1016/S0040-1951(98)00120-6.

Farquharson, J.I., Baud, P., Heap, M.J., 2017. Inelastic compaction and permeability evolution in volcanic rock. Solid Earth 8 (2), 561.

Folguera, A., Ramos, V.A., Melnick, D., 2003. Recurrencia en el desarrollo de cuencas de intra-arco. Cordillera Neuquina (37°300). Rev. Asoc. Geol. Argent. 58, 3–19.

Folguera, A., Ramos, V.A., Hermanns, R.L., Naranjo, J.A., 2004. e. Tectonics 23 (1–23), TC5008.

Folguera, A., Rojas-Vera, E., Vélez, L., Tobal, J., Orts, D., Agusto, M., Caselli, A., Ramos, V.A., 2016. A review of the geology, structural controls and tectonic setting of Copahue volcano, southern volcanic zone, Andes, Argentina. In: Tassi, F., Vaselli, O., Caselli, A.T. (Eds.), Copahue Volcano, Active Volcanoes of the World. Springer, pp. 3–22. https://doi.org/10.1007/978-3-662-48005-2_1.

Ghosh, N., Hatui, K., Chattopadhyay, A., 2019. Evolution of fault patterns within a zone of pre-existing pervasive anisotropy during two successive phases of extensions: an experimental study. Geo Mar. Lett. 40, 53–74. https://doi.org/10.1007/s00367-019-00627-6.

González, O., Vergara, M., 1962. Reconocimiento geológico de la Cordillera de Los Andes entre los paralelos 35° y 38° S, vol. 24. Universidad de Chile, Instituto de Geología, Publicación, p. 119.

Groeber, P., 1956. La Serie Andesítica patagónica. Sus relaciones, posición y edad. Rev. Asoc. Geol. Argent. 9, 39–42.

Groeber, P., Corti, H., 1920. Estudio geológico de las termas de Copahue. Estudio químico preliminar de las muestras de aguas recogidas en el terreno. Dirección General de Minas, Serie F, Informes Preliminares y Comunicaciones, Boletín 3, 1–20 (Buenos Aires).

Haberland, C., Rietbrock, A., Lange, D., Bataille, K., Hofmann, S., 2006. Interaction between forearc and oceanic plate at the south-central Chilean margin as seen in local seismic data. Geophys. Res. Lett. 33, 1–5. https://doi.org/10.1029/2006GL028189.

Heap, M.J., Violay, M.E.S., 2021. The mechanical behaviour and failure modes of volcanic rocks: a review. Bull. Volcanol. 83 (1), 1.

Heap, M.J., Wadsworth, F.B., Xu, T., Chen, C.F., 2016. The strength of heterogeneous volcanic rocks: a 2D approximation. J. Volcanol. Geoth. Res. 319, 1–11.

Henza, A.A., Withjack, M.O., Schlische, R.W., 2010. Normal-fault development during two phases of non-coaxial extension: an experimental study. J. Struct. Geol. 32, 1656–1667.

Henza, A.A., Withjack, M.O., Schlische, R.W., 2011. How do the properties of a pre-existing normal-fault population influence fault development during a subsequent phase of extension? J. Struct. Geol. 33, 1312–1324. https://doi.org/10.1016/j.jsg.2011.06.010.

Hervé, M., 1976. Estudio geológico de la falla Liquiñe-Reloncaví el área de Liquiñe: antecedentes de un movimiento transcurrente (Provincia de Vadivia). I Congreso Geológico Chileno (Santiago), Abstracts B 39–56.

Hervé, F., 1994. The southern Andes between 39° and 44°S latitude: the geological signature of a transpressive tectonic regime related to a magmatic arc. In: Reutter, K. J., Scheuber, E., Wigger, P.J. (Eds.), Tectonics of the Southern Central Andes. Springer, Berlin, pp. 243–248.

Hubbert, M.K., 1937. Theory of scale models as applied to the study of geologicstructures. GSA Bull 48, 1459–1520.

Huchon, P., Khanbari, K., 2003. Rotation of the syn-rift stress field of the northern Gulf of Aden margin. Yemen. Tectonophysics 364, 147–166.

JICA-EPEN (Japan International Cooperation Agency), 1992. The Feasibility Study on the Northern Neuquén Geothermal Development Project (Unpublished). Ente Provincial de Energía de la Provincia de Neuquén, p. 89.

Jordan, T.E., Burns, W.M., Veiga, R., Pangaro, F., Copeland, P., Kelley, S., Mpodozis, C., 2001. Extension and basin formation in the southern Andes caused by increased convergence rate: a mid-Cenozoic trigger for the Andes. Tectonics 20, 308–324. https://doi.org/10.1029/1999TC001181.

Kagan, Y.Y., 2005. Double-couple earthquake focal mechanism: random rotation and display. Geophys. J. Int. 164, 236–245. https://doi.org/10.1111/j.1365-246X.2005.

Kaverina, A.N., Lander, A.V., Prozorov, A.G., 1996. Global creepex distribution and its relation to earthquake-source geometry and tectonic origin. Geophys. J. Int. 125, 249–265. https://doi.org/10.1111/j.1365-246X.1996.tb06549.x.

Lamberti, M.C., Vigide, N., Venturi, S., Agusto, M., Winocur, D., Barcelona, H., Velez, M. L., Cardellini, C., Tassi, F., 2019. Structural architecture releasing deep-sourced carbon dioxide diffuse degassing at the Caviahue – copahue Volcanic Complex. J. Volcanol. Geoth. Res. 131–141. https://doi.org/10.1016/j.jvolgeores.2019.02.004.

Lara, L.E., Cembrano, J., Lavenu, A., 2008. Quaternary vertical displacement along the Liquiñe- Ofqui Fault Zone: differential uplift and coeval volcanism in the southern Andes? Int. Geol. Rev. 50, 975–993. https://doi.org/10.2747/0020-6814.50.11.975.

Lavenu, A., Cembrano, J., 1999. Compressional- and transpressional-stress pattern for Pliocene and Quaternary brittle deformation in fore arc and intra-arc zones (Andes of Central and Southern Chile). J. Struct. Geol. 21, 1669–1691. https://doi.org/10.1016/S0191-8141(99)00111-X.

Linares, E., Ostera, H.A., Mas, L., 1999. Cronología Potasio-Argón del complejo efusivo Copahue–Caviahue, Provincia de Neuquén. Rev. Asoc. Geol. Argent. 54 (3), 240–247.

Lepvrier, C., Fournier, M., Bérard, T., Roger, J., 2002. Cenozoic extension in coastal Dhofar (southern Oman): implications on the oblique rifting on the Gulf of Aden. Tectonophysics 357, 279–293.

Lundgren, P., Nikkhoo, M., Samsonov, S.V., Milillo, P., Gil-Cruz, F., Lazo, J., 2017. Source model for the Copahue volcano magma plumbing system constrained by InSAR surface deformation observations. J. Geophys. Res. Solid Earth 122 (7), 5729–5747.

Maccaferri, F., Rivalta, E., Keir, D., Acocella, V., 2014. Off-rift volcanism in rift zones determined by crustal unloading. Nat. Geosci. 7, 297–300.

Maccaferri, F., Richter, N., Walter, T., 2017. The effect of giant flank collapses on magma pathways and location of volcanic vents. Nat. Commun. 8, 1097.

Magee, M.E., Zoback, M.D., 1993. Evidence for a weak interplate thrust fault along the northern Japan subduction zone and implications for the mechanics of thrust faulting and fluid expulsion. Geology 21, 809–812.

Marrett, R., Allmendinger, R.W., 1990. Kinematic analysis of fault-slip data. J. Struct. Geol. 12 (8), 973–986.

Mas, L.C., 2010. History and Present Situation of the Neuquén Geothermal Project. Proceedings World Geothermal Congress. Bali, Indonesia, p. 2010.

Mas, G., Mas, L., Bengochea, L., 1995. Zeolite zoning in drill holes of the Copahue geothermal field, Neuquén, Argentina. In: Proceedings of the World Geothermal Congress, pp. 1077–1081.

Mas, G., Mas, L., Bengochea, L., 1996. Hydrothermal Surface Alteration in the Copahue Geothermal Field (Argentina). Proceedings 21st Workshop Geothermal Reservoir Engineering. Stanford University, California, SGP-TR, pp. 151–234.

McClay, K.R., White, M.J., 1995. Analogue modelling of orthogonal and oblique rifting. Mar. Petrol. Geol. 12, 147–151.

Melnick, D., Folguera, A., Rosenau, M., Echtler, H., Potent, S., 2002. Tectonics from the northern segment of the Liquiñe-Ofqui fault system (37°–39° S), patagonian Andes. V international symposium of andean geodynamics (toulouse). Extended Abstracts 413–417.

Melnick, D., Folguera, A., Ramos, V.A., 2006. Structural control on arc volcanism: the Copahue-Agrio complex, Central to Patagonian Andes transition (38°S). J. South Am. EarthSci. 22, 66–88.

Miyouna, T., Dieu-Veill Nkodia, H.M., Essouli, O.F., Dabo, M., Boudzoumou, F., Delvaux, D., 2018. Strike-slip deformation in the inkisi formation, brazzaville, republic of Congo. Cogent Geoscience 4 (1), 1542762.

Mon, R., 1987. Structural geology of two geothermal areas in the Andes: copahue and Tuzgle (Argentina). Bull. Eng. Geol. Environ. 35 (1), 79–85.

Montenegro, V.M., Spagnotto, S., Legrand, D., Caselli, A., 2021. Seismic evidence of the active regional tectonic faults and the Copahue volcano, at Caviahue Caldera, Argentina. Bull. Volcanol. 83, 20.

Morley, C.K., Harayana, C., Phoosongsee, W., Pongwapee, S., Kornsawan, A., Wonganan, N., 2004. Activation of rift oblique and rift parallel pre-existing fabrics during extension and their effect on deformation style: examples from the rifts of Thailand. J. Struct. Geol. 26, 1803–1829.

Nakamura, K., 1977. Volcanoes as possible indicators of tectonic stress orientation — principle and proposal. J. Volcanol. Geoth. Res. 2, 1–16. https://doi.org/10.1007/BF01637099.

Naranjo, J.A., Polanco, E., 2004. The 2000 AD eruption of Copahue volcano, southern Andes. Rev. Geol. Chile 31, 279–292.

Naylor, M.A., Mandl, G., Sijpesteijn, C.H.K., 1986. Fault geometries in basement-induced wrench faulting under different initial stress states. J. Struct. Geol. 8, 737–752.

Niemeyer, H., Muñoz, J., 1983. Hoja Laguna de La Laja, Región del Bío- Bío, escala 1: 250.000. Servicio Nacional de Geología y Minería.

Pardo-Casas, F., Molnar, P., 1987. Relative motion of the Nazca (farallon) and South-American plates since late cretaceous time. Tectonics 6, 233–248.

Pearce, R.K., Sánchez de la Muela, A., Moorkamp, M., Hammond, J.O.S., Mitchell, T.M., Cembrano, J., Araya-Vargas, J., Meredith, P.G., Iturrieta, P., Pérez-Estay, N., Marshall, N.R., Smith, J., Yáñez, G., Ashley-Griffith, W., Marquardt-Román, C.,

Stanton-Yonge, A., Núñez, R., 2020. Reactivation of fault systems by compartmentalized hydrothermal fluids in the Southern Andes revealed by magnetotelluric and seismic data. Tectonics 39, e2019TC005997. https://doi.org/10.1029/2019TC005997.

Pérez-Flores, P., Cembrano, J., Sanchez, P., Veloso, E., Arancibia, G., Roquer, T., 2016. Tectonics, magmatism and paleo-fluid distribution in a strike-slip setting: insights from the northern termination of the Liqui~ne-Ofqui fault System, Chile. Tectonophysics 680, 192e210. https://doi.org/10.1016/j.tecto.2016.05.016.

Pérez-Flores, P., Veloso, E., Cembrano, J., Sanchez-Alfaro, P., Lizama, M., Arancibia, G., 2017. Fracture network, fluid pathways and paleostress at the Tolhuaca geothermal field. J. Struct. Geol. 96, 134–148.

Pesce, A., 1989. Evolución volcano-tectónica del complejo efusivo Copahue–Caviahue y su modelo geotérmico preliminar. Rev. Asoc. Geol. Argent. 44, 307–327.

Petit, J.P., 1987. Criteria for the sense of movement on fault surfaces in brittle rocks. J. Struct. Geol. 9, 597–608.

Petrinovic, I.A., Villarosa, G., D'Elia, L., Guzmán, S.P., Páez, G.N., Outes, V., Manzoni, C., Delménico, A., Balbis, C., Carniel, R., Hernando, I., 2014. La erupción del 22 de diciembre de 2012 del volcán copahue, neuquén, Argentina: caracterización del ciclo eruptivo y sus productos. Rev. Asoc. Geol. Argent. 71 (2), 161–173.

Piquer, J., Yáñez, G., Rivera, O., Cooke, D., 2019. Long-lived crustal damage zones associated with fault intersections in the high Andes of Central Chile. Andean Geol. 46 (2), 223–239. https://doi.org/10.5027/andgeoV46n2-3106.

Radic, J.P., 2010. Las cuencas cenozoicas y su control en el volcanismo de los Complejos Nevados de Chillán y Copahue–Callaqui (Andes del Sur, 36–39 ° S). Andean Geol. 37, 220–246.

Rapela, C.W., Llambías, E.J., 1985. La secuencia andesítica terciaria de Andacollo, Neuquén, Argentina. Congreso Geológico Chileno 4, 458–488. Actas (Antofagasta).

Roman, A., Jaupart, C., 2014. The impact of a volcanic edifice on intrusive and eruptive activity. Earth Planet Sci. Lett. 408, 1–8. https://doi.org/10.1016/j.epsl.2014.09.016.

Rosenau, M., Melnick, D., Echtler, H., 2006. Kinematic constraints on intra-arc shear and strain partitioning in the southern Andes between 38 ° S and 42 ° S latitude. Tectonics 25, 1–16. https://doi.org/10.1029/2005TC001943.

Rojas-Vera, E., Folguera, A., Gímenez, M., Martínez, P., Ruiz, F., Ramos, V.A., 2008. Evolución tectónica de la fosa de Loncopué: estructura del depocentro cuaternario del Huecú y su relación con la sedimentación y el volcanismo. Rev. Asoc. Geol. Argent. 64 (2), 213–229.

Rojas-Vera, E., Folguera, A., Spagnuolo, M., Giménez, M., Ruiz, F., Martínez, P., Ramos, V.A., 2009. La neotectónica del arco volcánico a la latitud del volcán Copahue (38°S), Andes de Neuquén. Rev. Asoc. Geol. Argent. 65 (1), 204–214.

Roulleau, E., Bravo, F., Pinti, D., Barde-Cabusson, S., Pizarro, M., Tardani, D., de la Cal, F., 2017. Structural controls on fluid circulation at the Caviahue-Copahue Volcanic Complex (CCVC) geothermal area (Chile-Argentina), revealed by soil CO2 and temperature, self-potential, and helium isotopes. J. Volcanol. Geoth. Res. 341, 104–118.

Sánchez, P., Pérez-Flores, P., Arancibia, G., Cembrano, J., Reich, M., 2013. Crustal deformation effects on the chemical evolution of geothermal systems: the intra-arc Liquiñe–Ofqui Fault System. Southern Andes. Int. Geol. Rev. 37–41. https://doi.org/10.1080/00206814.2013.775731.

Schellart, W.P., 2000. Shear test results for cohesion and friction coefficients for different materials: scaling implications for their usage in analogue modelling. Tectonophysics 324, 1–16.

Sibson, R.H., 1996. Structural permeability of fluid-driven fault-fracture meshes. J. Struct. Geol. 18, 1031–1042. https://doi.org/10.1016/0191-8141(96)00032-6.

Sibson, R.H., Rowland, J.V., 2003. Stress, fluid pressure and structural permeability in seismogenic crust, North Island, New Zealand. Geophys. J. Int. 154, 584–594.

Siebert, L., 2002. Landslides resulting from structural failure of volcanoes. In: Catastrophic Landslides: Effects, Occurrence, and Mechanisms, 15. Geological Society of America, Boulder, CO, USA, pp. 209–235.

Sielfeld, G., Cembrano, J., Lara, L., 2017. Transtension driving volcano-edifice anatomy: insights from Andean transverse-to-the-orogen tectonic domains. Quat. Int. 1–17. https://doi.org/10.1016/j.quaint.2016.01.002.

Sierra, J., D'Amore, F., Panarello, H., Pedro, G., 1992. Reservoir characteristics of the vapour dominated geothermal field of Copahue, Neuqu'en, Argentina, as established by isotopic and geochemical techniques. Geothermal Investigations with Isotope and Geochemical Techniques in Latin America. In: Proceedings of Nuclear Techniques in Geothermal Resources Investigation, pp. 13–30. San Jose, Costa Rica.

Sinclair, I.K., 1995. Transpressional inversion due to episodic rotation of extensional stresses in Jeanne d'Arc Basin, offshore Newfoundland. In: Buchanan, J.G., Buchanan, P.G. (Eds.), Basin Inversion, vol. 88. Geological Society Special Publication, pp. 249–271.

Somoza, R., 1998. Updated Nazca (Farallon) - south America relative motions during the last 40 My: implications for mountain building in the Central Andean region. J. S. Am. Earth Sci. 11, 211–215.

Somoza, R., Ghidella, M.E., 2012. Late Cretaceous to recent plate motions in western South America revisited. Earth Planet Sci. Lett. 331, 152–163.

Sruoga, P., Consoli, V., 2011. Volcán Copahue. Relatorio Congreso Geológico Argentino, Neuquén.

Stanton-Yonge, A., Griffith, W.A., Cembrano, J., St Julien, R., Iturrieta, P., 2016. Tectonic role of margin-parallel and margin-transverse faults during oblique subduction in the southern volcanic zone of the Andes: insights from boundary element modeling. Tectonics 35, 1990–2013.

Suárez, M., Emparan, C., 1997. Hoja Curacautín, Regiones de la Araucanía y del Biobío. Servicio Nacional de Geología y Minería, Carta Geológica de Chile 71, 105 mapa 1: 250.000.

Sveen, J.K., 2004. An Introduction to MatPIV V. 1.6.1. User Reference Manual, p. 27.

Tardani, D., Reich, M., Roulleau, E., Takahata, N., Sano, Y., Pérez-Flores, P., Sánchez, P., Cembrano, J., Arancibia, G., Sánchez-Alfaro, P., Cembrano, J., Arancibia, G., Sa, P., Sano, Y., Pe, P., Arancibia, G., 2016. Exploring the structural controls on helium, nitrogen and carbon isotope signatures in hydrothermal fluids along an intraarc fault system. Geochim. Cosmochim. 184, 193–211. https://doi.org/10.1016/j.gca.2016.04.031.

Tassi, F., Agusto, M., Lamberti, C., Caselli, A., Pecoraino, G., Caponi, C., Vaselli, O., 2017. The 2012–2016 eruptive cycle at Copahue volcano (Argentina) versus the peripheral gas manifestations: hints from the chemical and isotopic features of fumarolic fluids. Bull. Volcanol. 79 (10), 69.

Thielicke, W., Stamhuis, E., 2014. PIVlab–towards user-friendly, affordable and accurate digital particle image velocimetry in MATLAB. J. Open Res. Software 2 (1), 30. https://doi.org/10.5334/jors.bl.

Thomson, S., 2002. Late Cenozoic geomorphic and tectonic evolution of the Patagonian Andes between latitudes 42S and 46S: an appraisal based on fission-track results from the transpressional intraarc Liquiñe-Ofqui fault zone. Geol. Soc. Am. Bull. 114 (9), 1159–1173.

Tibaldi, A., 2005. Volcanism in compressional tectonic settings: is it possible? Geophys. Res. Lett. 1033 (32), L06309.

Tron, V., Brun, J.P., 1991. Experiments on oblique rifting in brittle-ductile systems. Tectonophysics 188, 71–84.

van Mechelen, J.L.M., 2004. Strength of moist sand controlled by surface tension for tectonic analogue modeling. Tectonophysics 384, 275–284.

Varekamp, J.C., Ouimette, A.P., Herman, S.W., Flynn, K.S., Bermudez, A., Delpino, D., 2009. Naturally acid waters from Copahue volcano, Argentina. Appl. Geochem. 24 (2), 208–220.

Vélez, M.L., Euillades, P., Caselli, A.T., Blanco, M., Martínez-Díaz, J., 2011. Deformation of Copahue volcano: inversion of InSAR data using a genetic algorithm. J. Volcanol. Geoth. Res. 202, 117–126.

Vélez, M., Euillades, P., Blanco, M., Euillades, L., 2016. Ground Deformation between 2002 and 2013 from Insar observations.Copahue Volcano. Springer, 175–198.

Veloso, E.E., Tardani, D., Elizalde, D., Godoy, B.E., Sanchez-Alfaro, P.A., Aron, F., Reich, M., Morata, D., 2019. A review of the geodynamic constraints on the development and evolution of geothermal systems in the Central Andean Volcanic Zone (18–28° Lat. S). Int. Geol. Rev. 62 (10), 1294–1318.

Ventura, G., Vilardo, G., Bruno, P.P., 1999. The role of flank failure in modifying the shallow plumbing system of volcanoes: an example from Somma-Vesuvius. Italy. Geophys. Res. Lett. 26, 3681–3684.

Wallace, R.E., 1951. Geometry of shearing stress and relation to faulting. J. Geol. 59, 118–130.

Wang, K., Hu, Y., Bevis, M., Kendrick, E., Robert, S., Vargas, R.B., Lauría, E., Smalley, R., Vargas, R.B., Lauría, E., 2007. Crustal motion in the zone of the 1960 Chile earthquake: detangling earthquake-cycle deformation and forearc-silver translation. G-cubed 8, 1–14. https://doi.org/10.1029/2007GC001721.

Watanabe, T., Masuyama, T., Nagaoka, K., Tahara, T., 2002. Analog experiments on magma-filled cracks. Earth Planets Space 54, 1247–1261.

White, D.J., Take, W.A., Bolton, M.D., 2001. Measuring Soil Deformation in Geotechnical Models Using Digital Images and PIV Analysis. Proceedings of the 10th International Conference on Computer Methods and Advances in Geomechanics, Tucson, Arizona.

Withjack, M.O., Jamison, W.R., 1986. Deformation produced by oblique rifting. Tectonophysics 126, 99–124.

Yagupsky, D.L., 2010. Metodología para el estudio de sistemas compresivos y sus controles estructurales. Tesis Doctoral, FCEN, UBA. Inédita.

Yagupsky, D.L., Cristallini, E.O., Fantín, J., Zamora Valcarce, G., Bottesi, G., Varadé, R., 2008. Oblique half-graben inversion of the mesozoic neuquén rift in the malargüe fold and thrust belt, mendoza, Argentina: new insights from analogue models. J. Struct. Geol. 30, 839–853.

Yáñez, G., Gana, P., Fernández, R., 1998. Origen y significado geológico de la Anomalía Melipilla, Chile central. Rev. geológica Chile.

Yin, Z.M., Ranalli, G., 1993. Determination of tectonic stress field from fault slip data: toward a probabilistic model. J. Geophys. Res. 98, 12 165–12 176.